UNIVERSITY OF COIMBRA
FACULTY OF SCIENCE AND TECHNOLOGY

CRITICAL HEALTH S.A.

Fovea and Optic Disk Detection and Key Performance Indicators Process Automation

José Manuel Neves Pinão

Coimbra, July 2011

"A journey of a thousand miles begins with a single step." - Lao Tzu

Contents

List of Figures

List of Tables

Acknowledgements

I want to express my gratitude to several people with special importance during this enriching learning experience.

I would like to express my gratitude to my colleagues at Critical Health, for sharing the team spirit and the good environment along this year in particular to João Pinto, Frederico Teles, André Lemos and Tânia Baptista but especially to Carlos Manta Oliveira, my supervisor, for the continuous guidance, patience and friendship.

I am also grateful to João Diogo Ramos for the opportunity to develop this final work in Critical Health.

Thanks to Nuno C. Ferreira for helping me reviewing this document.

For my friends, thanks for all the enriching adventures and support to my professional and personal challenges.

Last, but not least, my deepest thanks to my parents and sister for the unconditional support during my life and for allowing me to achieve who I am today.

Abstract

This work, integrated in Critical Health, presents a new process to detect fovea and optic disk in retinal images and the application of some technologies to do the automation of Key Performance Indicators process (KPI).

The proposed method consists in five steps: selection of an area in the image where the optic disk is located using Sobel operator, extraction of optic disk boundaries applying the Hough transform to detect center and diameter of optic disk, detection of the ROI (region of interest) where the fovea is located based on the optic disk center and its diameter and detection of the fovea within the ROI. The developed algorithm has been tested in a proprietary dataset with 1464 images (with ground truth generated by experts) and with some public datasets.

Retmarker is an image processing product developed by Critical Health. The KPI is a process implemented in Critical Health to test Retmarker with the goal to reach the optimal performance. This process is currently highly manual and performed on a weekly basis, demanding a considerable amount of man-hours per year. A new plan was implemented to make this process fully automated.

Keywords: Biomedical image processing, Digital images, Filtering, Image segmentation, Anatomical structure, Automation, Database systems.

Chapter 1

Introduction

1.1 Context

Presently, the diabetic population is estimated to be 200 millions people. It is expected a growth until 360 million in 2030. As consequence of diabetes, several pathologies have a high probability to affect the retina. Diabetic retinopathy is responsible for 4.8% of the 37 million cases of blindness around the world [**?**] .Glaucoma is the second leading cause of blindness in the world. Age-related macular degeneration, increasingly frequent in older adults, currently affects 30 millions of people [**?**].

Digital imaging and computer processing resources have been improving every year. The potential of this resource is huge in all fields of medicine such as ophthalmology. Nowadays there are automated diagnostic systems to follow the evolution of some diseases whose symptoms become visible in the fundus eye. Diabetic retinopathy and age related macular degeneration are some of the diseases that can be detected and followed in retinography images. Furthermore the diameter changes of the retinal vessels are an indicator of cardiovascular system problems.

Retmarker is a Critical Health's solution to monitor the progression of retinal diseases. This product allows a detailed analysis, using non-invasive imaging methods, of several retinal pathologies and it is supported on the certification of the company's Quality Management System according to the "EN ISO 13485:2003 + AC:2007" and "EN ISO 9001:2008" standards.

1.2 Scope of the Work

In order to this product to become an efficient solution, each of the modules needs to have the best performance possible regarding:

- Time.
- Accuracy.
- Automations.

However, there is some margin to improve the modules. Critical Health developed a process to improve the accuracy of Retmaker algorithms. Key Performance Indicators are a group of metrics used to assess the Retmarker performance. The scripts to calculate them are regularly executed to analyse the performance levels of each kind of processing with the goal of reaching the best performance. However this process actually needs a long time due to some steps which require human intervention to complete the results generation.

This work has two main goals:

- Improve the module of fovea and optic disk detection.
- Plan and put in practice an automation plan for Key Performance Indicators.

1.3 Report Overview

This report is organized as follows: chapter 2 gives a brief overview regarding the vision system describing the main structures and the eye behavior. Also the main diseases that affect the fundus eye are mentioned.

Chapter 3 describes the main approaches present in the existent literature as well the limitations of each one. Presently there are 6 main approaches identified in literature: blood vessels tracing, template matching, active counter or snakes, machine learning, multilevel threshold and shape detection.

The new method developed in this work to detect fovea and optic disk in retinography images is detailed in the chapter 4.

The actual state and the automation plan implemented for the Key Performance Indicators process is explained in the chapter 5.

Chapter 6 is divided in two main sections. The first one presents the results reached for the proposed model to do the detection of the fovea and optic disk. The second describe the implementation of the plan to automate the Key Performance Indicators process.

Finally, chapter 7 summarizes the conclusion and the future work.

The appendices present further details of the automation scheme implemented for the Key Performance Indicators process.

Chapter 2

The Eye

This chapter begins an overview about the anatomy and physiology of the vision system. The main pathologies of the retina are also mentioned. This section also describes the main principals about the use of retinography images.

2.1 Anatomy and Physiology

The eye is an organ with the ability to convert light into electro-chemical impulses. These impulses then go to the brain where they are interpreted and create the notion of shapes, colors, and dimensions of objects in the world.

The process of vision begins with the light coming in the eye through the cornea. The cornea is an external clear layer at the front of the eye. After it there is a progression to the pupil. The pupil is located in the central region of the iris that controls the amount of light entering the eye by dilating or constricting the pupil. The iris is the structure that assigns the eye's color. The light reaches then the crystalline lens that focuses it in the retina. Ciliary muscles control the shape's lens. For a close object, the lens becomes rounder, otherwise it becomes flat (figure 2.1).

The retina is a layer responsible for converting the light into electro-chemical impulses. This structure is filled by specialized photoreceptor cells (figure 2.2). There are 2 types of photoreceptors: rods and cones. Between 6 and 7 million of cones provide the eye's color sensitivity. They are much more concentrated in the macula, zone responsible for the central vision. The rods are the most numerous of the photoreceptors, about 120 million, and are more sensitive that the cones. However, they are not sensitive to color.

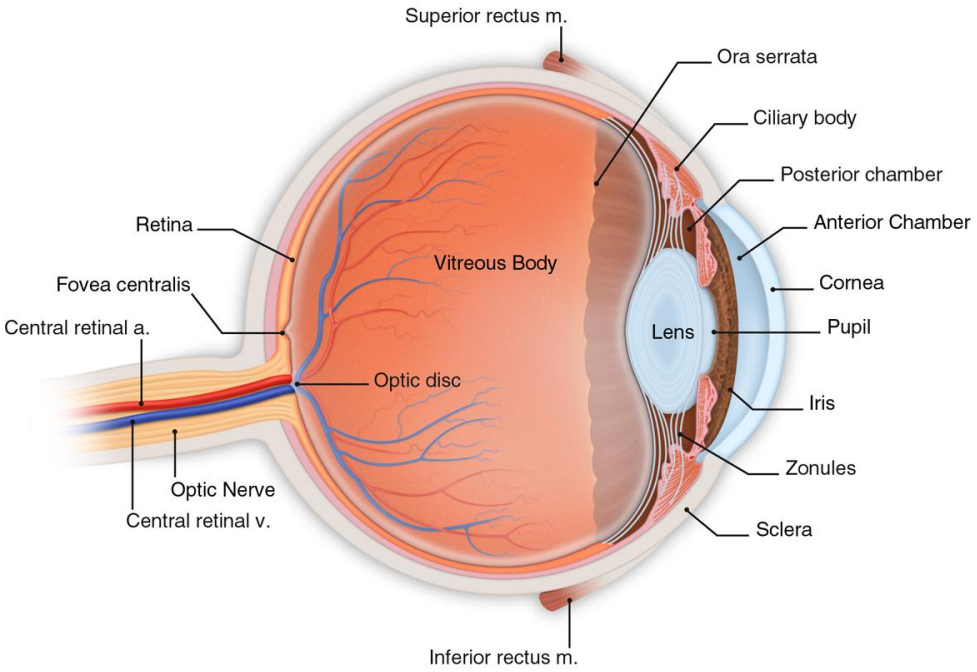

Figure 2.1: Eye anatomy scheme [?].

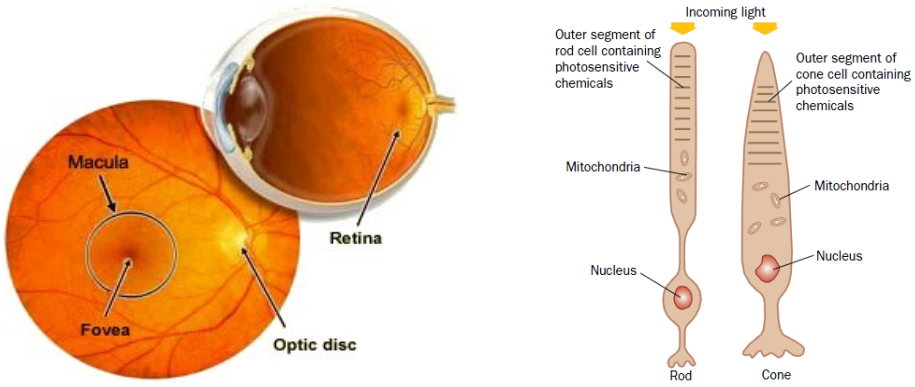

(a) Retina's surface.

(b) Basic structure of rods and cones.

Figure 2.2: The retina [?] [?].

They are responsible for our dark-adapted vision. The impulses generated by these cells go throw the optic nerve until the brain. The optic disk is the exit point of the optic nerve from the retina and continues beyond it. On the

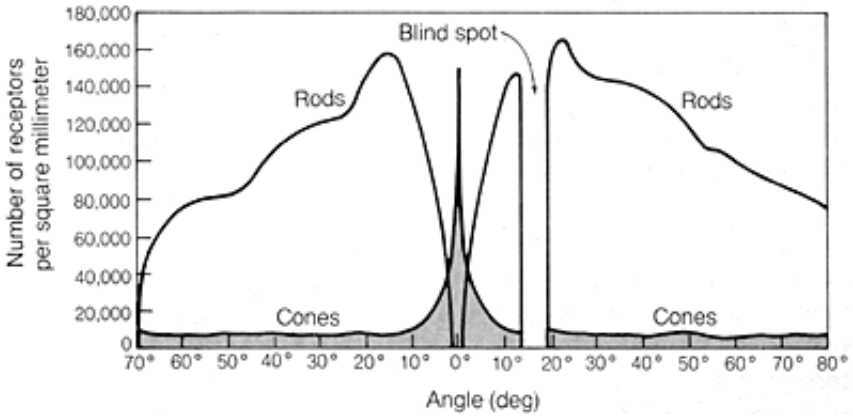

Figure 2.3: Rods and cones distribution [?].

other hand is the entrance and the exit point for retinal blood vessels. The optic disk is the structure responsible by the blind spot (figure 2.3). This area does not respond to any light stimulation because there are no photoreceptors on it. Each eye transmits a slightly different inverted image which is combined and corrected when its signals reach the brain. [?] [?] [?]

2.2 Retinal Pathologies

The eye can suffer several disorders that can change the appearance of the retina. There are three typical main diseases that can affect this structure causing the vision loss:

- Diabetic retinopathy.
- Glaucoma.
- Age related macular degeneration (AMD).

People with diabetes have a considerable probability to suffering of diabetic retinopathy. This disease degrades the tiny vessels in the retina and causes the uncontrolled generation of the new ones (figure 2.4a). The new tiny vessels can grow ahead of the retina and occlude the light causing vision damage. The diabetic retinopathy gives no warning until the first damages occurs and cause vision loss. The retinography images are the main process to check if there are signals of this disease. The main signals are the formation of microaneurysms, growth of abnormal blood vessels that cause frequently

(a) Advanced stage of diabetic retinopathy.

(b) Treatment with photocoagulation.

Figure 2.4: Retinal images of diabetic retinopathy.

hemorrhages and accumulations of lipids (exudates). The treatment for this disease consists in burning some locations in the retina keeping untouched the macula to maintain the central vision. This process is known as focal laser photocoagulation (figure 2.4b) [**?**].

Glaucoma is a disorder of the optic nerve that cause a irreversible loss of vision. One typical symptom is the high pressure in the eye due of excess of intraocular fluid. This excess happens due to the incapacity of the fluid to leave the eye while the production continues. This increased fluid pressure pushes the optic nerve back into a concave shape (figure 2.5). Other symptom is the tunnel vision due of the loss of the peripheral vision. [**?**]

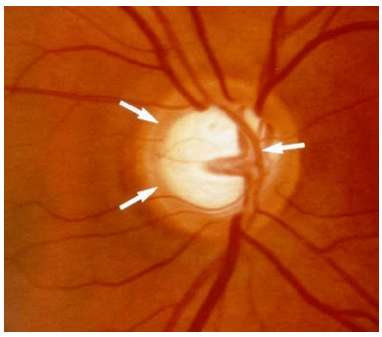

Figure 2.5: Concave shape in an optic disk of an eye with glaucoma [**?**].

Age related macular degeneration is a disease that can destroy the central vision. The main risk factor is the age. There are two types of AMD: dry and wet (figure 2.6). The dry is characterized for the presence of drusens (yellow deposits) in the retina but with no loss of vision in a early stage. In the advanced stage the drusens have a bigger size and there is loss of vision due of the degradation of the light-sensitive cells. On the other hand, the wet is more severe and less common. It is characterized for the tight junctions of the vessels. This effect causes leaks and bleeding that cause a retinal deformation what causes the loss of vision rapidly. [?] [?] [?]

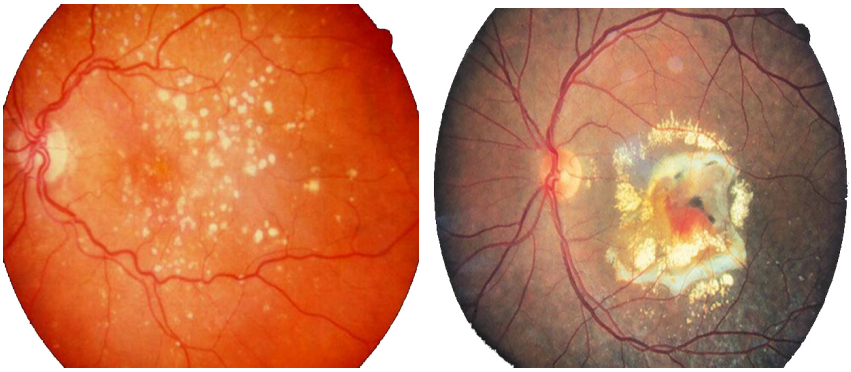

(a) Dry AMD. **(b)** Wet AMD.

Figure 2.6: Age related macular degeneration types [?].

2.3 Retinography Images

Every year there are advances in image processing and an increase of the computers power. All the medicine fields have been taking advantage of this fact. Ophthalmology is heavily dependent of the visual signs analyses. The retinography images are records of the retina in-vivo and allow the visualization and analysis of its state. The retina is the unique body's location where the vessels are observed without any invasive techniques. This fact allows to easily calculate the arterio-venous ratio which is an important indicator of the heart diseases and the stroke risk [1]. Nowadays there are systems which offer high-resolution images for all clinical scenarios. As digital data have the advantage of easy storage without loss of quality with time, can be easily sent through short or long distances. Actually, the image processing methods allow an automatic diagnostic of the patients using this kind of images.

This work is directed for field 1 and field 2 retinography images. The field 1 images are centered in the optic disk and the field 2 centered in the fovea (figure 2.7)

(a) Field 1. **(b)** Field 2.

Figure 2.7: Retinography image fields.

Chapter 3

Detection's Approaches

Fovea and optic disk are important structures present in retinography images. These structures have a special importance in image processing of this kind of images due to use as landmarks as well as the necessity of proceeding to their occlusion to improve the performance of other kind of processings. On the other hand, changes near of the fovea indicates loss of vision. The next section gives an overview of the methodologies existent in the literature and its limitations as well.

3.1 Blood Vessel Tracing

Blood vessels are observed in the retinography images crossing the optic disk coming in by the up side and going out by the down side. Its convergent point locates inside the optic disk. Some models find this point estimating the blooad vessels orientation. This approach was followed by *Foracchia et al* [7] which estimates two parabolas where the intersection is admitted like a point in the optic disk (figure 3.1).

Hoover and *Goldman* [9] created a method to detect the optic disk with a fuzzy convergence of the blood vessels. The fuzzy convergence is applied initially to find the origin point of the vessels present in an image. A cloud of candidates (figure 3.2) is generated and the peak of darkness will be admitted as the convergence point.

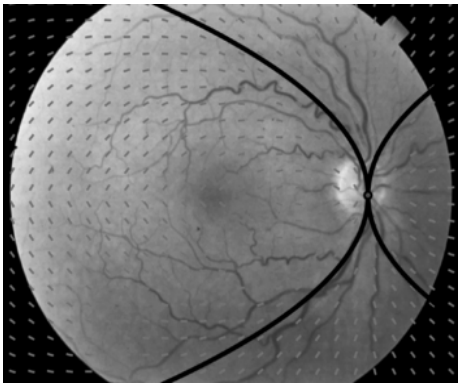

Figure 3.1: Parabolas drawn with the Foracchia model [7].

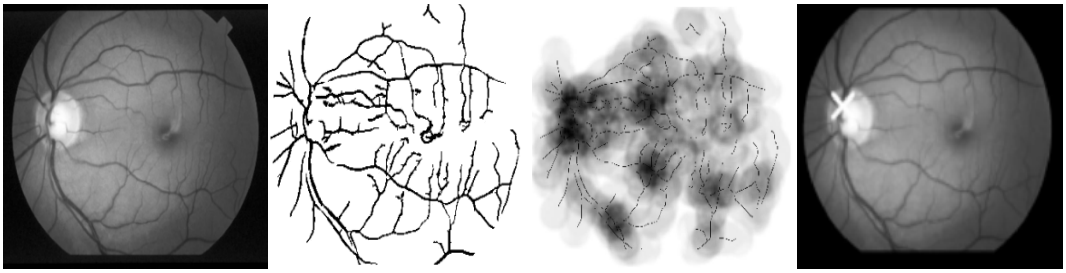

(a) Source image. **(b)** binary image with the segmented vessels. **(c)** Fuzzy convergence of blood vessels. **(d)** Optic disk detected.

Figure 3.2: Convergent point of blood vessels detected with the Hoover methodology [9].

3.2 Template Matching

Template matching is a method in image processing used to classify different objects or portions of images against one another. *Lalond et al* [12] developed a methodology based in the template matching to locate the optic disk combination two procedures:

1. Hausdorff-based template matching technique on edge map.
2. Pyramidal decomposition for large scale object tracking (figure 3.3).

The application of these two models generates candidates that need to be classified with the Dempster–Shafer. The best candidate classified is elected as the optic disk.

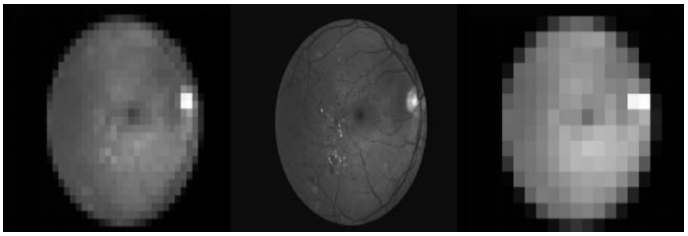

(a) **(b)** **(c)**

Figure 3.3: Piramidal decomposition model used to segment the brightest regions [12].

Jelinek et al [10] developed a method where a combination of Butterworth filtering, canny edge detection and morphological filters are used.

Youssif et al [25] created initially a vessels mask (figure 3.4b). All remaining vessel-labeled pixels that are not within a 41 41 square centered on each of the highest 4% intensity pixels in the illumination equalized image are relabeled as nonvessel pixels generating an image of candidates (figure 3.4c). The image of candidates is then matched with a filter describing the expected appearance of a desired region containing the optic disk. The best match is elected the optic disk region.

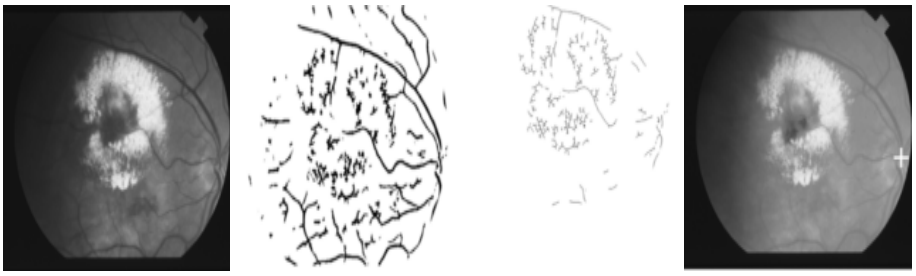

(a) Source image. **(b)** Binary vessel/non-vessel image. **(c)** Final OD-center candidates. **(d)** Optic disk detected.

Figure 3.4: Detection of the convergent point with the Youssif's model [25].

3.3 Active Contour or Snake

Active contours simulate a curve that evolves a structure of interest detected by the energy on its boundaries. The snakes have the capacity to move dynamically in the image space and use the mass density to detect the desired boundary. For a good orientation a damping coefficient that characterizes the medium where the snake moves needs to be well attributed. The final position of the snake will depend of some parameters like the initial position, velocity, mass density, the damping coefficient, and influences of the image itself like lines and edges. The snake can follow any contour of interest since there is the right combination between the knowledge about the object of interest, as the optic disk, and the individual image characteristics, in this case the fundus eye.

Mendels et al [14] created a method based in a snake to detect the optic disk boundary (figure 3.5). To put in practice the snake algorithm, a heavy pre-processing of the images was necessary to becomes the optic disk edge more continue and minimize the vessels effect in the boundary. A grey level morphology was used to reach this stage.

Figure 3.5: Convergent solution of a GVF-based snake used by Mendel. The snake was influenced by the edges created by blood vessels [14].

Osareh et al [17] improved the previous algorithm using a Lab colour space. They reached a better homogeneous optic disk boundary applying the grey level morphology in [14] but with the lightness channel L of the HLS colour space, colour morphology using the full HLS space, and two variations of colour morphology using the Lab space.

Chanwimaluang et al [3] developed an algorithm with two steps. The first estimates the optic disk center finding the higher local variance. Once the dark blood vessels cross the bright optic disk the higher variance should be inside the optic disk boundary [20]. In the second step is applied a snake algorithm the detect the boundary [24].

3.4 Machine Learning

The machine learning methods are mathematical models where there is a computational learning. It consists in a design and development of algorithms that allow computers to evolve behaviors based on empirical data. The learning takes the advantage of capture characteristics of interest doing the recognition of complex patterns.

Sinthanayothin et al [20] proposed an algorithm based on a neural network to detect the main structures of the retinography images (optic disk, fovea and blood vessels) and features of glaucoma, senil macular degeneration and diabetic retinopathy such hemorrhages and exudates. The bright optic discs were located by identifying the area with the highest variation in intensity of adjacent pixels due to be crossed by the dark blood vessels. A multilayer perception classifies each pixel of the image as a vessel or non-vessel. The foveas were identified using matching correlation together with characteristics typical of a fovea.

Chutatape et al [4] applied a PCA method on each pixel after to select the candidate region based on the clustering of the brightest pixels. The PCA with different scaling factors was applied on each candidate region to find the minimum distance between the input image and its projection onto the disk space. The optic disc center is admitted like the least distance in the candidate regions among all the scaling factors.

Li et all [13] created a boundary detection of optic disk based on a modified ASM method to be more robust and faster that the original suggested by *Cootes and Tayler* [5] mainly in cases where the edge is weak or too much occluded by blood vessels. In a first step, principal component analysis detects the optic disk. Then, the result of PCA initializes the ASM to detect the disk boundary (figure 3.6).

Niemeijer et al [15] proposed a model to determine the location of a set of points in an image. This model needs a set of images to be trained with

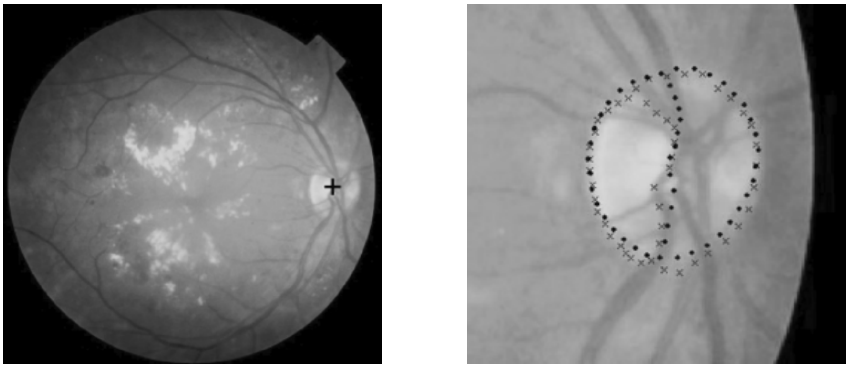

(a) PCA. **(b)** ASM.

Figure 3.6: PCA and ASM results using the ASM method developed by Li [13].

a point-distribution-model (PDM), proposed by *Cootes et al* [5] (figure 3.7). After the points are all positioned in the input image is possible estimate the location of the optic disk, macula and the vascular arch. The first and second point locate optic disk and macula, 3-6 the optic disk boundary and the others the vascular arch.

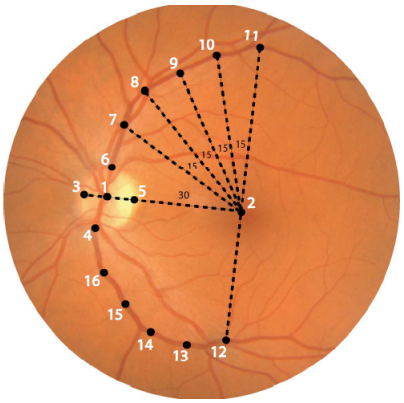

Figure 3.7: Niemeijer's Model overlaid on a retinal image [15].

Tobin et al [22] developed a Bayesian classifier that assumes a multivariate normal distribution model to classify the pixels in the original image into the binary category of optic nerve or not optic nerve.

3.5 Multilevel Thresholding

Thresholding is a technique for image segmentation which tries to identify and extract a structure from its background or texture in image objects. The key parameter in the thresholding process is the choice of the threshold value. One of the simpler methods to choose a threshold can be a mean or median value. Others sophisticated approach resort to histograms for select a value of a peaks or valleys. Others resort to clustering where gray-level samples are clustered in two parts as background and object. Otsu's method [18] is probably the most known way to find a threshold in images having a bi-modal histogram. However, the retinography images have multimodal histograms due the presence of many features such as arteries, veins, optic disc, fovea, exudates and even noise. Hence a multilevel thresholding method has to be employed to extract the optic disc and exudates in retinal images.

Kavitha and Devi [11] created a three step method to detect exudates and the optic disk. The first one detects the vessels location and its convergent point using a least square polynomial curve. The second step uses a multilevel thresholding methodology to detect the brighter regions on the image as optic disk and exudates. To determine the multilevel threshold of each image efficiently, *Kavita and Devi* proposed the valley-seeking approach which find the local minimum (valley) in a histogram as a threshold. The local minima are fond admitting that the histogram's equation of the image is given by h(i) where i is an integer, $g_{min} \leq i \leq g_{max}$ where g_{min} is the minimum and g_{max} is the maximum of the gray level in the image. The condition is:

$$\begin{aligned} V = \{(i, h(i)) \mid [(h(i) < h(i-1) \& (h(i) \leq h(i+1)) or \\ (h(i) \leq h(i-1) \& h(i) < h(i+1))], g_{min+1} \leq i \leq g_{max-1}\} \end{aligned} \tag{3.1}$$

After all the small valleys are detected, they are removed and the grey level of the last one is selected as the threshold value. The image is then segmented with the selected threshold and brighter regions are found. The bright region having the convergent point of the blood vessels is elected the optic disk.

3.6 Shape Detection

Shape detection algorithms are used in image segmentation to detect objects with a predefined shape of interest.

Sekhar et al [19] applied the popular Hough transform to locate the circular optic disk. To reduce the possibility of an erroneous detection, in the instance is selected a region of interest (ROI). The ROI is selected using morphology operations to find the brightest region of the image. The main morphologic operations used were:

Dilation

$$(f \oplus B) = max\{f(x-s, y-t)|(s,t)\epsilon B\} \tag{3.2}$$

Erosion

$$(f \ominus B) = min\{f(x+s, y+t)|(s,t)\epsilon B\} \tag{3.3}$$

Opening

$$(f \circ B) = (f \ominus B) \oplus B \tag{3.4}$$

Closing

$$(f \cdot B) = (f \oplus B) \ominus B \tag{3.5}$$

Reconstruction

$$\rho f(g) = V_{n\geq 1} \partial_f^{(n)}(g) \tag{3.6}$$

The Hough transform characterizes the image into a parameter space which it is constructed specifically to describe the desired shape analytically. To detect circles, its parametric form is:

$$(x-a)^2 + (y-b)^2 = r^2 \tag{3.7}$$

where a and b is the center and r the radius of the circle. The Hough space has three parameters:

- Center.
- Radius.
- Accumulator.

each parameter combination is accumulated in a accumulated array, The highest peak indicate the most circular shape.

(a) Image 01 of STARE [**?**]. **(b)** Edges of Sobel operators. **(c)** Successfully detected OD.

Figure 3.8: Xiaolu et al method [26].

Xiaolu et al [26] developed a method to apply the Hough transform on an image pre-processed with *Sobel* [**?**] [**?**] and *Canny* [2] operators (figure 3.8). *Canny* proposed an approach based in the multidirectional derivatives, multiscale analysis, and optimization procedures to do a good edge detection. Obtaining a binary edge map of the image based on these operators, Hough transform provides a reliable detection of the most circular shape in that image.

3.7 Limitations

All methodologies described above have some limitation. The approaches based in the blood vessels tracing, snakes, and machine learning need a long processing time. Moreover, the simple application of the blood vessels tracing does not enable to detect the optic disk radius or the boundary. On the other hand, machine learning needs a huge training sample to cover an acceptable level of the real possibilities. The Hough transform, typically used to detect lines and circles, has the problem of the optic disk not being a perfect circle but singly elliptic. It can be adapted to detect ellipses. However it becomes computationally too heavy.

Chapter 4

Fovea and Optic Disk Methodology

A new methodology is proposed to do a reliable fovea and optic disk detection with a capacity to detect the center and radius of the optic disk and the location of the fovea. This approach is based in the shape detection where is done initially a pre-processing and then applied the Hough transform to find optic disk. Fovea is detected admitting that is located at two and a half optic disk radius from its center [20].

4.1 Pre-Processing

In this first step, the source image is corrected for a series of errors until a stage is reached where it is possible apply the Hough transform with reliable results. The following steps are the key for the good detection with the Hough transform in this model. All the images processed are resized, by setting the height to 576 pixels while keeping the aspect ratio.

4.1.1 Noise attenuation

The retinal fundus is an irregular surface where exists gradients beyond the vessels, optic disk and fovea that affect the application of the Hough transform causing an erroneous detection. All the source image is smoothed with a dynamic implemented average filter. This filter starts with a strong smoothing effect due a large kernel (9 x 9). The kernel size is being reduced until there is gradient detected by the sobel operator.

4.1.2 Sobel operator

The sobel operator calculates the gradient of the source image intensity at each pixel [**?**]. This operator detects the horizontal or vertical gradient depending of the implemented derivative kernel version:

$$G_y = \begin{bmatrix} 1 & 2 & 1 \\ 0 & 0 & 0 \\ -1 & -2 & -1 \end{bmatrix} * A \qquad G_x = \begin{bmatrix} 1 & 0 & -1 \\ 2 & 0 & -2 \\ 1 & 0 & -1 \end{bmatrix} * A \tag{4.1}$$

After the low-pass filter application, the sobel operator detects the image gradient.

where A represents the source image and * denotes the 2-dimensional convolution operation. The combination is reached calculating the gradient magnitude:

$$g = \sqrt{G_x^2 + G_y^2} \tag{4.2}$$

Additionally the gradient direction (Θ) can be estimated calculating the angle between the two gradients:

$$\Theta = \arctan\left(\frac{G_x}{G_y}\right) \tag{4.3}$$

where Θ represents the angle of the gradient. The image processed is three dimensional where the peaks represent the high transition areas. According with the ETDRS retinography protocol [**?**], the OD in field 1 and 2 is located in a horizontally centered region. The majority of the undesired gradient formed due of the vessels is masked in this step. Figure 4.1 shows an image of reasonable quality processed with sobel operator which optic disk area has a peak due of the transition between the dark blood vessels crossing the bright optic disk.

Sobel operator with vessels mask

This model has two tested versions. The first one consists in the simple application of the sobel operator and the other in a combination between the sobel operator and a vessels mask. The vessels mask is described later in the subsection 4.1.5. The second version is modified by appying the sobel operator in the vicinity of the blood vessels. In practice , the sobel operator is performed to the whole image and set to zero in regions far from the detection vessels.

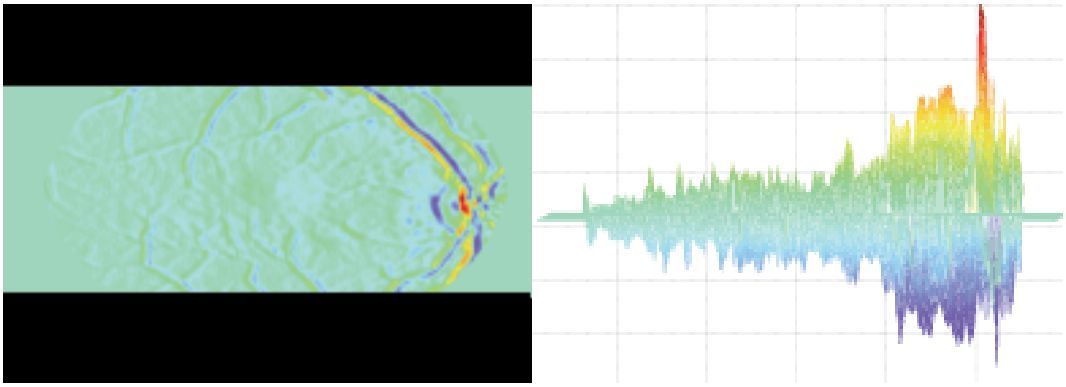

(a) Top view (Gradient's image masked). **(b)** Side view.

Figure 4.1: 3D view of the Sobel operator gradient.

4.1.3 Find region of interest

In order to define the ROI for the OD detections, the sobel operator is performed only in the red channel of the image. To the results of the sobel operator, a kernel is applied with a size of 31,25% from the image which sums the values of the each image region. The peak of this sum is admitted like containing the optic disk. If the source image is field 2, the optic disk is located near of the margins. In these cases, the ROI does not intercept the center of the image and will have an area of 25% (Figure 4.2) of the image size. Otherwise the ROI keeps a size of 31,25% (Figure 4.3).

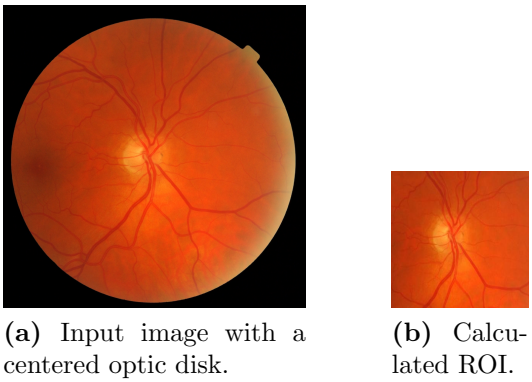

(a) Input image with a centered optic disk. **(b)** Calculated ROI.

Figure 4.2: Result for a centered optic disk.

(a) Input image with a peripheral optic disk.

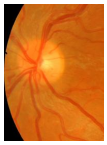

(b) Calculated ROI.

Figure 4.3: Result for a peripheral optic disk.

4.1.4 Gauss gradient

The Gaussian filter (Figure 4.4b) is considered as the optimal filter for image smoothing. This filter is applied on images using the two dimension version. It consists of the product of two one-dimension Gaussians [8], one for the x axis and the other for the y:

$$g(x,y) = \frac{1}{2\pi\sigma^2} e^{-\frac{x^2+y^2}{2\sigma^2}} \tag{4.4}$$

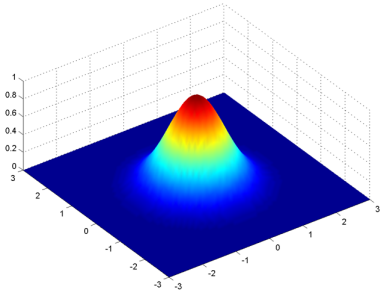

(a) 2-D function.

0.02	0.08	0.14	0.08	0.02
0.08	0.37	0.61	0.37	0.08
0.14	0.61	1.0	0.61	0.14
0.08	0.37	0.61	0.37	0.08
0.02	0.08	0.14	0.08	0.02

(b) 2-D kernel (size 5x5 and $\sigma = 1.0$).

Figure 4.4: Gaussian filter.

In this step is calculated the Gaussian gradient using the first order derivative of the Gaussian function. The goal is to control the width of the boundary between the background and the foreground to improve the performance of the Hough transform (figure 4.5).

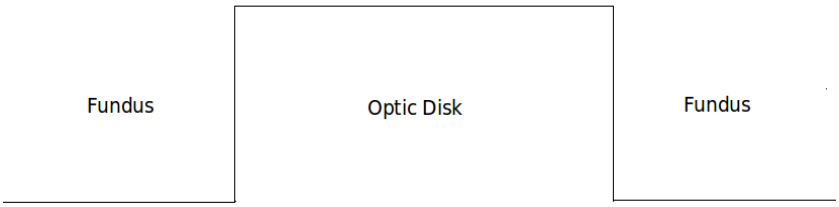

(a) Ideal scheme of the optic disk and the background intensities.

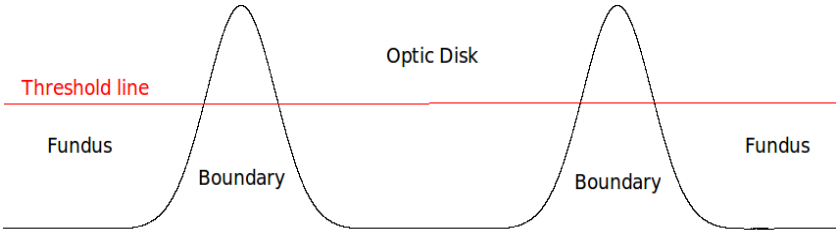

(b) Isolation of the optic disk boundary after to apply the gaussian gradient.

Figure 4.5: Gaussian gradient effect

Two parameters define the derivative Gaussian kernel: the standard deviation (σ) which control the width of the Gaussian function and the kernel size (Figure 4.6).

The derivative Gaussian filter is then applied to each color channel individually and only the maximum for all channels in each position is considered. The image of gradient is then normalized with the adaptive contrast enhancement transformation initially proposed by *Sinthanayothin et al* [20] defined bellow:

$$f(i,j) \rightarrow g(i,j) = 255 \frac{[\Psi_W(f) - \Psi_W(f_{min})]}{[\Psi_W(f_{max}) - \Psi_W(f_{min})]} \tag{4.5}$$

where W(i, j) is a subimage of size MxM pixels centred on a pixel located at (i, j). The sigmoid function is defined as:

$$\Psi_W(f) = \left[1 + exp\left(\frac{< f >_W - f}{\sigma_W}\right)\right]^{-1} \tag{4.6}$$

and f_{max} and f_{min} are the maximum and minimum of intensity in the image with:

$$f >_{W(i,j)} = \frac{1}{M^2} \sum_{(h,l)\epsilon W(i,j)} f(h,l) \tag{4.7}$$

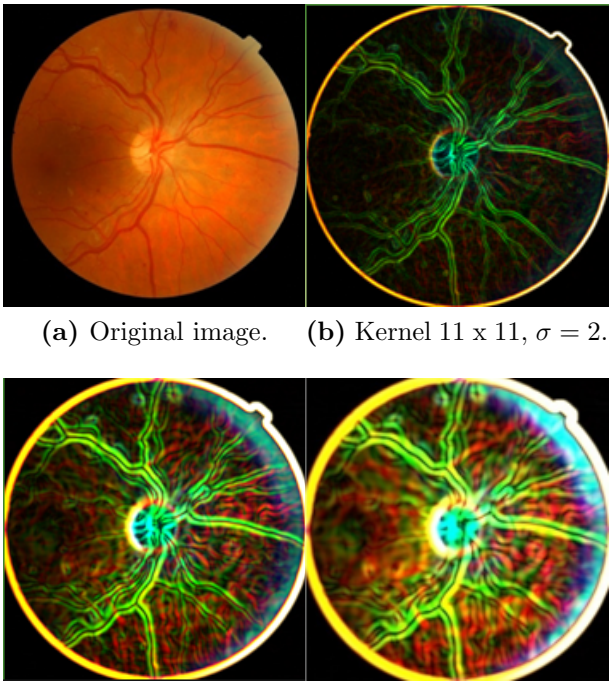

(a) Original image. **(b)** Kernel 11 x 11, $\sigma = 2$.

(c) Kernel 19 x 19, $\sigma = 4$.**(d)** Kernel 25 x 25, $\sigma = 6$.

Figure 4.6: Exemple of an image processed with different derivative Gaussian kernels.

$$\sigma_W^2(f) = \frac{1}{M^2} \sum_{(k,l)\epsilon W(i,j)} (f(k,l) - < f >_W)^2 \tag{4.8}$$

The normalized image is then binarized with a threshold reached using the Otsu's method [18]. A kernel with a $\sigma = 2$ and a size of 11 x 11 was applied in this step due there is a peak of performance for the Hough transform (described in the next section) with this values.

4.1.5 Vessels detection

The structures detected applying the Gaussian gradient are the optic disk and the blood vessels. In this work, the blood vessels are removed using a median filter. This filter rank all the values matched with an image and replace its center with the value of the ranking's center (Figure 4.7).

The blood vessels are long and thin structures. The thin feature is the key for the use of this filter. If the kernel is large enough comparing with

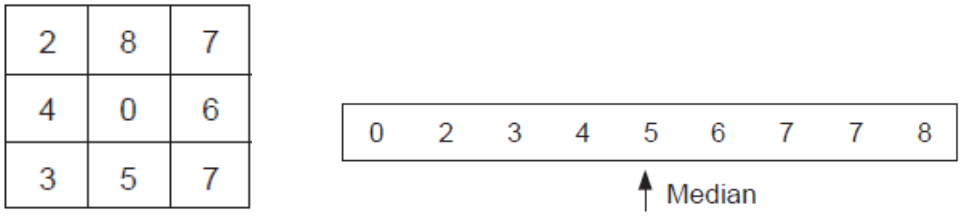

(a) 3 x 3 template. **(b)** Sorted vector.

Figure 4.7: Median Filter. [**?**]

the width of the blood vessels, all the vessel points will be located before the center of the ranking vector. Hence, the result will be an image with the vessels overshadowed. Subtracting the original ROI with the ROI with the vessels overshadowed an image is obtained with the vessels trace (Figure 4.8).

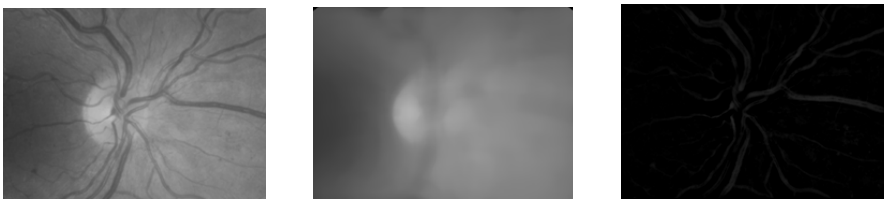

(a) Gray scale ROI. **(b)** ROI with vessels overshadowed. **(c)** Subtraction.

Figure 4.8: Obtaining vessels.

The image generated from the subtraction has typically bad quality and needs some adjustments to become useful. This image is normalized with the same method described in the Gaussian gradient section. After that, the image is binarized with the threshold equal to the median of the gray scale ROI (Figure 4.9).

The binarized ROI reached from the Gaussian gradient is then subtracted by the ROI with the binarized vessels slightly dilated and the structures smaller then 500 pixels are deleted. The result is an image significantly cleaner (Figure 4.10).

(a) Subtracted image.

(b) Subtracted image enhanced.

Figure 4.9: Vessels enhancement.

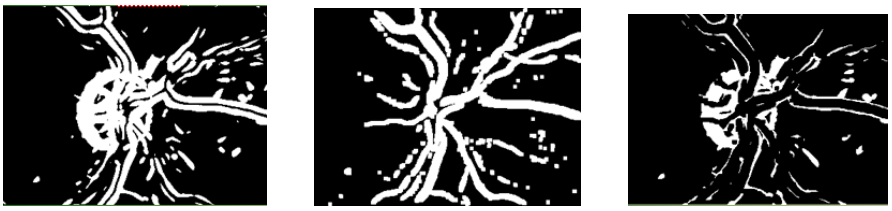

(a) Binarized ROI from Gaussian gradient.

(b) Binarized ROI with blood vessels.

(c) Subtracted ROI.

Figure 4.10: ROI cleaner.

4.1.6 Image quantization

This last step will perform the quantization of the ROI to reach a binary image only with the optic disk boundary. Prior to this operation, the gray scale ROI is normalized following the same principle detailed in the gaussian gradient section. The optic disk ROI is then quantized in 32 distinct intensity levels. Some of them will correspond to some levels of the optic disk. From studying tests was found that the optic disk boundary typically has an intensity between 87,5% and 71% of the full scale after the quantization. Hence all the areas with a intensity higher then 87,5% are set to zero. Also the pixels with intensity lower than 71% are set to zero to remove some undesired artefact as the residues of vessels. All the corresponding areas erased in this step are erased in the binary ROI (figure 4.11). This step improves significantly the performance of the algorithm.

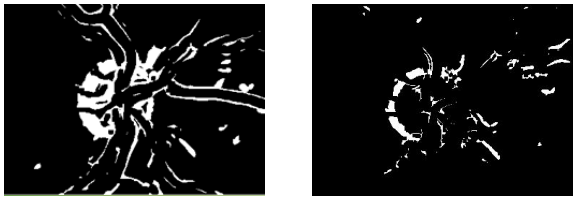

(a) Before. **(b)** After.

Figure 4.11: ROI cleaning with the Quantization step

4.2 Hough transform

The Hough transform is a technique to detect shapes in images. This transform is used mainly to extract lines from a similar mathematical definition of the Radon transform [6] and circumferences. For this case, this transform was implemented with the goal of detect circular shapes. The equation of the circumference is defined by:

$$(x - x_0)^2 + (y - y_0)^2 = r^2 \tag{4.9}$$

where x and y are a locus of the points, x_0 and y_0 are the origin coordinates and r the radius. Each edge point present in the input image defines a set of circles. All circles defined for one edge point are centered on it and fill all range possible of radius. Each edge point of one defined circle in the source image will origin a circle that will intersect the others from the other edge points in the center (figure 4.12)

(a) Binary image with a circle.

(b) Circle detection process.

Figure 4.12: Hough transform for circles [**?**].

The three parameters for each circle (center and radius) are stored in the

accumulator space. For the image of figure 4.14a there will be a peak in the accumulator corresponding to the position of the center and the radius of the circle. The equation for the circle (Equation 4.9) can be redefined as:

$$x = x_0 + r\cos(\theta) \qquad y = y_0 + r\sin(\theta) \tag{4.10}$$

The Hough space is then defined reorganizing the equation as:

$$x_0 = x + r\cos(\theta) \qquad y_0 = -r\sin(\theta) \tag{4.11}$$

where depends of the radius r and the angle θ. The peaks will happen in the points where exist more intersections that will be in the center of each circle of the source image. Figure 4.13 shows 2 example of accumulators where is observed a tolerance of noise and occlusion.

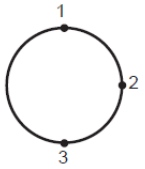

(a) Clean image.

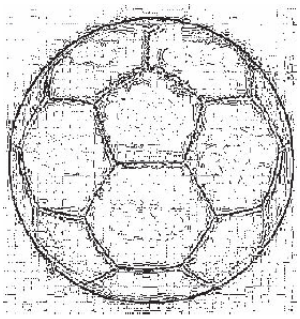

(b) Image with noise.

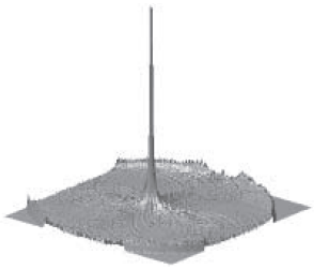

(c) Accumulator of the clean image.

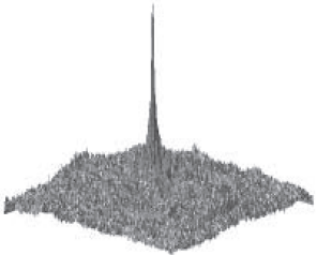

(d) Accumulator of the image with noise.

Figure 4.13: Noise tolerance to Hough transform [**?**].

The Hough transform is finally applied on the pre-processed image to detect the most circular shape corresponding of the optic disk (Figure 4.14). This transform was implemented with a limitation regarding the radius length to detect. A minimum and maximum radius were defined analysing the

ground truth of the proprietary dataset which one has all the images with a size of 768 x 576, the same size of the resize step. The minimum represents the first percentile (43 pixels) and the maximum the last (64 pixels).

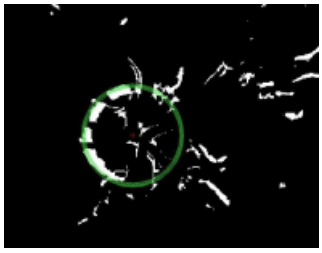

(a) ROI of the pre-processed image.

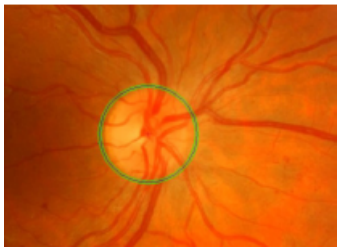

(b) ROI of the source image.

Figure 4.14: Optic disk detection using the Hough transform.

4.3 Fovea detection

Located in the center of the macula, fovea is a dark point at 2.5 diameters of the optic disk from its center [20]. Initially is calculated the circumference centered in the optic disk with 2.5 optic disk radius (Figure 4.15a). The image is then masked and only a region of interest will be uncovered (Figure 4.15b). This algorithm is tailored to process images of field 1 or field 2, so the fovea will be more or less a half heigh of the image.

It is admitted that the fovea location is the center of the darkest square of dimensions 11 x 11 in the region of interest in the source image resized. Finally, the output is the source image with the fovea and optic disk successfully detected. Figure 4.16) shows the optic disk marked with a blue circumference and the fovea with the green star.

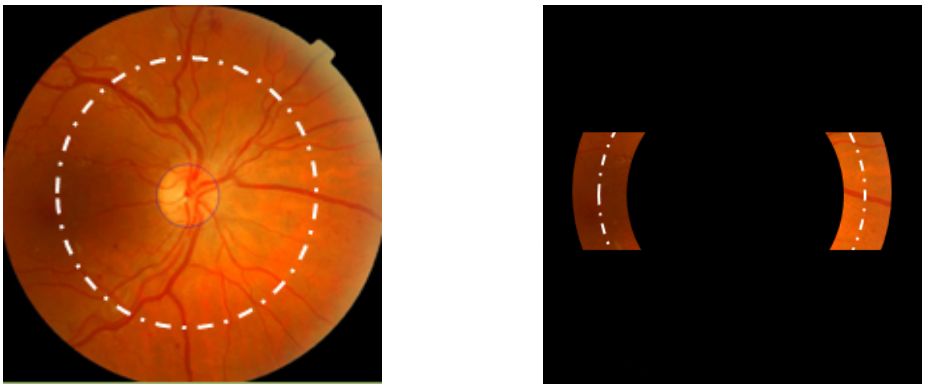

(a) Distance calculation. **(b)** Mask.

Figure 4.15: Region of interest of the fovea.

Figure 4.16: Fovea and optic disk successfully detected.

Chapter 5

Key Performance Indicators

5.1 Current State

Retmarker is constituted by five main modules:

- Differences.
- Microaneurysms detection.
- Registration.
- Vessels detection.
- Fovea and optic disc detection.

These modules are regularly tested with the goal of improving the performance of each one. There are scripts to start the process containing the thresholds to be settled. The modules are tested with some datasets and the results compared with ground truth generated by experienced physicians. The final parameters generated regarding the performance of each module are called by Key Performance Indicators (KPI). The whole process is highly manual and needs a long time to be finished. The process starts with a simple matlab script which calls the five main modules of the Retmarker. The results are then saved in text files. The content of this files needs then to be copied to an excel sheets where the results are compiled to generate some parameters such as sensibility and specificity. Moreover, the comparison between processes with different dates is very difficult to do. Therefore it is complicated analysing the history of the performance.

The KPI for detection of differences between images consists in three main categories: Pixel level, region level and frame level (Table 5.1). Pixel level are the lower level statistics of the three ones and is about the position of the pixels detected as difference. Region level is regarding the position of the stains of pixels marked as differences. The frame level is the statistic regarding the quantity of pixels stains marked as difference in the whole image.

Pixel level	Sensitivity
	Specificity
	False positives / Number of images
Frame level	Sensitivity
	Specificity
	False positives / Number of images
Region level	Sensitivity
	False positives / Number of images

Table 5.1: KPI for detection of differences.

The statistics for microaneurysms and vessels detection consists in a simple comparison between the detection of the Retmarker and the ground truth on pixels level (Table 5.2).

Sensitivity
Specificity
False positives / Number of images

Table 5.2: KPI for microaneurysms and vessels detection.

The statistics generated for the performance of fovea and optic disc detection (Table 5.3), are based in the euclidean distance between the location of the fovea and the center of the optic disk with the coordinates present in the ground truth for the dataset of test. This comparison uses a threshold previously defined as an euclidean distance of 20 pixels in images of 768 x 576. If the location for these structures is a distance less than the threshold, the detection is admitted as with success. Regarding the optic disk radius, the threshold consists in a value to compare with the quotient between the radius detected and the respective radius present in the ground truth. If the

quotient is belong to]0.9 1.1[the radius was successful detected. Moreover, it is yet calculated the number of foveas successfully detected after the optic disk, once that the fovea detection is based in the detected position of the optic disk center in the image.

Fovea mass center
Optic disk mass center
Optic disk heigh ratio
Fovea mass center with success in optic disc

Table 5.3: KPI for fovea and optic disk detection.

The registration module consists in two different algorithms: V1 and V2. The V1 is slower but has a higher level of success that the V2. The KPI consists in three different types (Table 5.4). The first shows the performance for V1 algorithm, the second the performance for V2 and the last does a comparison between both. Individually, for V1 and V2 are generated the quantity of images successfully and unsuccessfully registrable, the accuracy of the registry based in a threshold previously defined, and the mean accuracy for each one. The two algorithms were compared generating the number of images where each one has the best performance comparatively, where V1 fails the register and V2 was successful, where V2 fails the register and V1 had success and finally where the two algorithms fail the register.

Registration V1	Best Registration
	Accuracy < thr
	Registration Fail
	Mean Accuracy
Registration V2	Best Registration
	Accuracy < thr
	Registration Fail
	Mean Accuracy
V1 and V2 Fail	
V2 Fail and V1 Register	
V1 Fail and V2 Register	

Table 5.4: KPI for registration module.

5.2 Planning

The first step for the automation consists in to build an interface dedicated to start the process. Some useful requirements were implemented:

- Send an e-mail up to three different addresses warning when the processing ends via gmail.
- Create a root output folder for the output files of all modules.
- Delete possible existing cache.
- Export results to the database.
- Save and load settings.
- Generate automatically a script called from a batch file that runs in the windows task schedule.
- Save a log written by the user to easily identify the process.

Retmarker needs some days to generate all the results. When the results are generated, they are stored in an appropriate database.

An application developed in C# (object-oriented language based on C++) should be build to analyze the KPI easily. This application uses SQL queries to access the database and automatically compare the parameters between each processing and shows an overall analysis of all of them. This application allows the user to access the data regarding the processings exported to the database for each Retmarker's module. It should grant an easy search by processing ID, processing date or log and delete database data. Also there is the possibility to export a pdf report with the results of a selected processing (Appendix A)

Chapter 6

Results

6.1 Fovea and Optic Disk Detection

Two matlab prototypes were built and tested. The first one defines the region of interest using only the sobel operator. This first approach manifested some problems to detect the mentioned structures in images with several lesions presents in the public Stare dataset. In order to improve the detection for this kind of images, the second prototype uses a combination between the sobel operator and the vessels mask (chapter 4, section 4.1).

The first prototype was tested with a proprietary dataset and with four public datasets. The second one was only tested with the public Stare dataset. The performance was compared with the actual algorithm integrated in Retmarker for fovea and optic disk detection (Reference). All the tests were performed in a machine with 2.83GHz Intel Core 2 quad CPU and 1.98Gb of RAM.

6.1.1 Datasets

The proprietary dataset consists in 1464 non-midriatic anonymous images from a Diabetic Retinopathy Screening Programme in Portugal. The public datasets used for the validation of this algorithm are:

- Messidor [**?**].
- ROC [**?**].
- Drive [**?**].
- Stare [**?**].

Messidor dataset has been established to facilitate studies on computer-assisted diagnoses of diabetic retinopathy. This dataset contain 1200 eye fundus color numerical images acquired by 3 ophthalmologic departments using a color video 3CCD camera on a Topcon TRC NW6 non-mydriatic retinograph with a 45 degree field of view. Each one was captured using 8 bits per color plane at 1440*960, 2240*1488 or 2304*1536 pixels.

ROC dataset has 100 images all taken from patients with diabetes without known diabetic retinopathy. The images were taken with Topcon NW 100, NW 200 or Canon CR5-45NM 'non-mydriatic' cameras at the default resolution and compression settings. The images are a random sample of all patients that were noted to have red lesions from a large ($>$ 10,000 patients) diabetic retinopathy screening program, and each image is from a different patient.

Regarding Drive dataset, the photographs were obtained from a diabetic retinopathy screening program in The Netherlands. The screening population consisted of 400 diabetic subjects between 25-90 years of age. Forty photographs have been randomly selected, 33 do not show any sign of diabetic retinopathy and 7 show signs of mild early diabetic retinopathy. Each image has been JPEG compressed. The camera used was a Canon CR5 non-mydriatic 3CCD with a 45 degree field of view. Each image was captured using 8 bits per color plane at 768 by 584 pixels.

Stare dataset is constituted by 81 images: 31 healthy retinas and 50 containing pathological lesions of various types and severity. This dataset has been widely tested in literature.

6.1.2 Assessments for the proprietary dataset

The proprietary dataset is the only one with ground truth information on fovea and optic disk positions generated by experienced physicians. The analysis between the reference and the proposed method with the proprietary dataset was based in the euclidean distance between the location of the optic disk center and fovea detected by each algorithm and the ground truth.

As all the images have the dimension of 768 x 576, was admitted that if the euclidean distance between the optic disk or fovea detected and the respective coordinates in ground truth was less then 20 pixels, these structures were successfully detected. Regarding the optic disk radius, the evaluation was based in the quotient between the radius detected by each algorithm and

the respective radius in the ground truth. If this quotient belonged to the interval]1 - 0.1 ; 1 + 0.1[the radius was admitted as correctly detected. Also the processing time was evaluated.

	Developed Code nº of images (%)	**Reference** nº of images (%)
Optic Disk Mass center (euclidean distance < 20 pixeis)	1259 (86,00%)	1001 (68,37%)
Optic Disk height (ratio ε]1 - 0.1 ; 1 + 0.1[)	912 (62,30%)	526 (35,93%)
Fovea Mass Center (euclidean distance < 20 pixeis)	1265 (86,41%)	966 (65,98%)
Average Processing Time by Image	10,9452 s	12,1176 s

Table 6.1: Results for the proprietary dataset.

Table 6.1 shows the results for the proprietary dataset. The proposed method achieved a better detection in all fields. The optic disk center reached a success rate 17,63% higher than the reference. The optic disk radius and fovea was detected with 26.37% and 20.43% higher respectively. The analysis of the following accumulative charts shows a continue increase of performance of the proposed method comparing with the reference for the optic disk center (Figure 6.1 and the fovea 6.2). This charts compare the detection levels for different values of threshold.

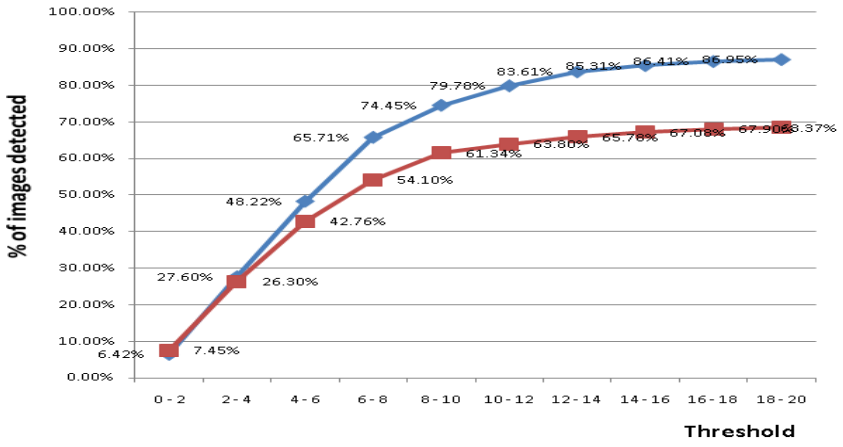

Figure 6.1: Accumulative chart for the optic disk center detection.

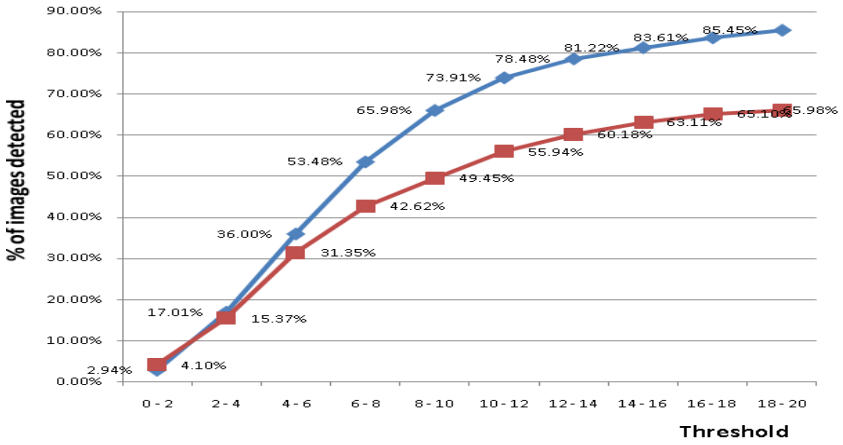

Figure 6.2: Accumulative chart for the fovea detection.

The chart in figure 6.1 shows an increase of performance since the euclidean distance of three pixels. Similarly, analyzing the chart in figure 6.2 is observer since the threshold of two for the fovea. The following histograms obtained with SPSS [?] shows a visual impression of the distribution of data. The total area of the histograms is equal to the number of data.

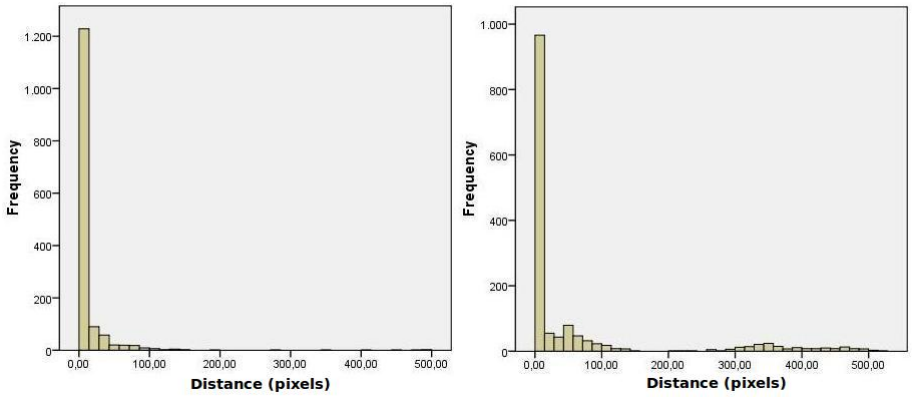

(a) Developed Algorithm. **(b)** Reference.

Figure 6.3: Frequency histogram showing the distribution of the euclidean distances between the detected optic disks and the ground truth for each algorithm.

Figure 6.3 shows two histograms with the frequency of the euclidean distance sample for the proposed method in figure 6.3a and for the reference

in figure 6.3b regarding the optic disc. Analysing this charts is observed a higher trend of the sample present in the chart 6.3a to be closer of the origin and a smaller number of outliers. The mean of the euclidean distances for the sample created by the developed algorithm is equal to 13,82 and the standard deviation to 34.592 pixels. On the other hand the reference presents a mean of 63.64 and a standard deviation of 124,733 pixels. This data indicates that there is a higher dispersion of the sample generated by the reference. The same evidence is observed in relation to the fovea in figure 6.4.

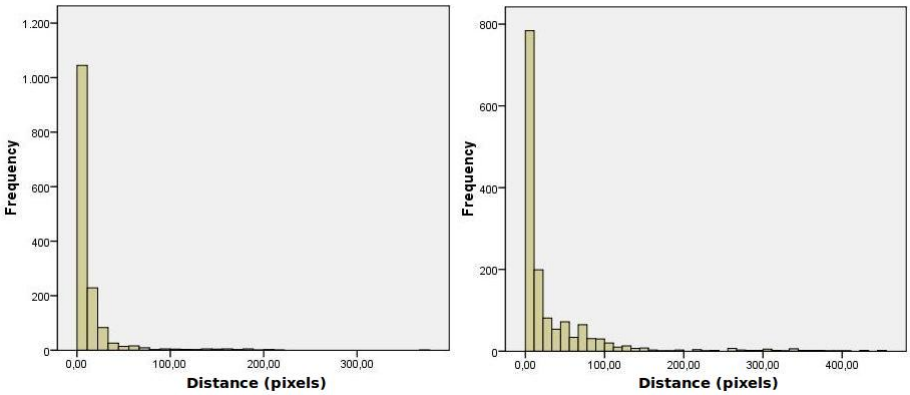

(a) Developed Algorithm. **(b)** Reference.

Figure 6.4: Frequency histogram showing the distribution of the euclidean distances between the location of foveas and the ground truth for each algorithm.

In this case the mean and the standard deviation are respectively 14,67 and 26.887 pixels for the sample created by the developed method. Reference presents a mean of 34,69 and a standard deviation of 61,699. These facts mean that there is a significant decrease of the sample amplitude for both methods comparing with the optic disk case.

The following figures show 2 histograms with the quotients samples regarding the radius for the proposed method and the reference. The sample of the proposed model in figure 6.5a seams a tight Gaussian function with a peak centered in 1 which means a good performance. On the other hand the histogram for the reference (Figure 6.5a) shows two peaks where no one is centered in 1. A boxplot of this samples were generated for each one. This kind of plot depicts groups of numerical data through their five-number summaries with an easy way to understand: the smallest observation (min-

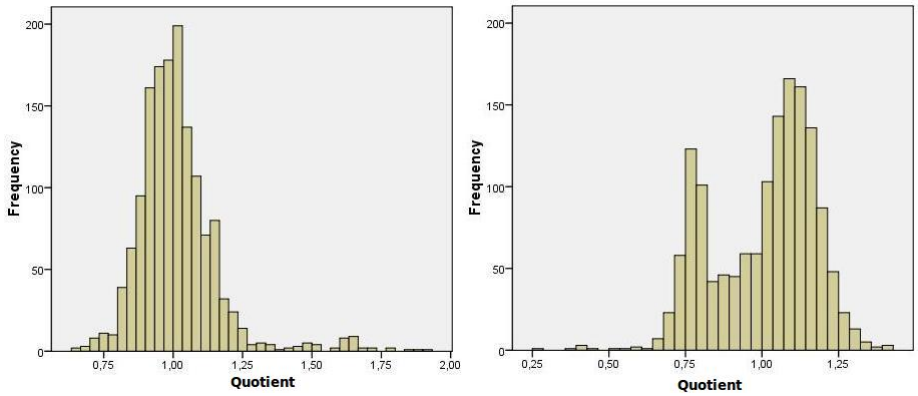

(a) Developed Algorithm. **(b)** Reference.

Figure 6.5: Frequency histogram showing the distribution of the quotient between the estimated radius of each optic disk and the respective radius in the ground truth.

imum), 25º quartile, median, 75º quartile, and largest observation (maximum). Notwithstanding, also the outliers are easily represented if there are any (Figure 6.6).

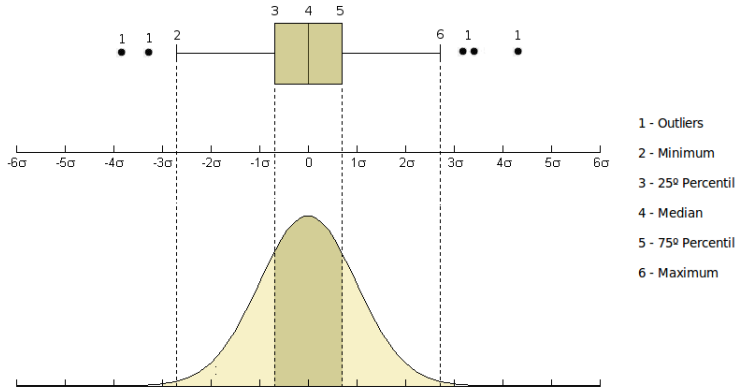

Figure 6.6: Box-and-Whisker Plot scheme.

In figure 6.7 is quite perceptible the larger amplitude of the reference sample in the second quartile (Figure 6.7b) and a median further from 1. Moreover, it's observed a trend for there to be outliers mainly after the maximum for the sample of the developed model (Figure 6.7a). The outliers in the reference sample are all located before the minimum. All this indicators conclude that the developed model has a higher accuracy then the reference about the estimation of the optic disc radius.

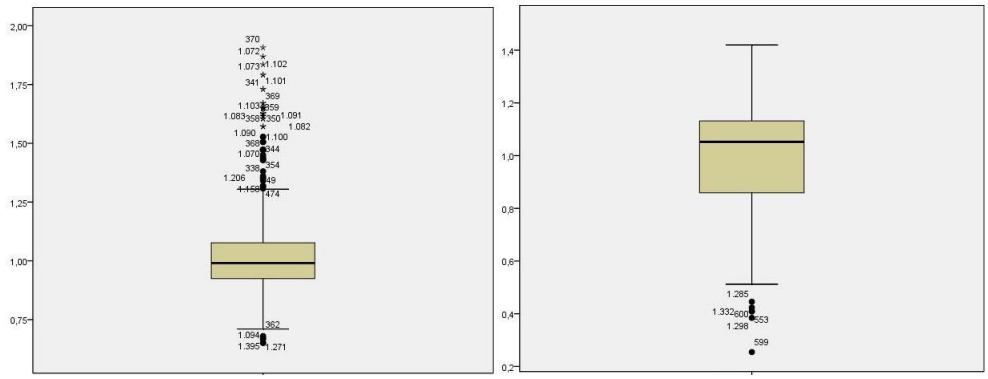

(a) Developed Algorithm. **(b)** Reference.

Figure 6.7: Boxplot regarding optic disk radius for 2 methods.

6.1.3 Assessments for the public datasets

All the public datasets tested do not have ground truth. The results were generated only for the optic disk detection admitting that if the optic disk center was detected inside the optic disk boundary, the detection was successful. The results for all this datasets are in the following table:

Dataset	**Optic disk detected**	
	Developed Code	**Reference**
Messidor	1156 (96,33%)	488 (40,67%)
ROC	98 (98,00%)	96 (96,00%)
Drive	39 (97,50%)	39 (97,50%)
Stare	47 (58,02%)	59 (72,84%)

Table 6.2: Results for the public datasets.

Observing the table 6.2 the developed model presents a better accuracy for the majority of the datasets tested. This difference is higher for the Mes-

sidor which indicates a high performance for this kind of images. The images of the Stare dataset have particular features. A lot of images of this dataset has brighter structures due of some diseases like exudates or drusens. It is evident some difficulties of the algorithm to detect the mentioned structures in this kind of images. A slightly modification was implemented in the model. A combination between the sobel operator with the vessels mask (chapter 4) was implemented to find the region of interest. Table 6.3 compare the reference, the two versions of the model and the methods tested with this dataset presents in the literature.

Optic disk detection methods	**Stare dataset**
Highest average variation - Sinthanayothin et al [20]	42.0%
Largest brightest connected objects - Walter and Klein [23]	58,0%
Average OD-images model - based - Osareh et al [16]	58,00%
Proposed method using only the sobel operator to find the ROI	**58,00%**
Resolution pyramid using a simple Haar-based discrete wavelet transform - Frank ter Har [21]	70,4%
Hausdorff - based template matching, piramidal decomposition & confident assignment Lalond et al [12]	71,6%
Hough transform applied only to pixels close to the retinal vasculature - Frank ter Har [21]	71,6%
Reference	**72,8%**
Proposed method with the combination between the sobel operator and the vessels mask to find the ROI	**74,1%**
Fuzzy convergence - Hoover and Goldbaum [9]	89,0%
Fitting the vasculature orientation on a directional model - Frank ter Har [21]	93,8%
A geometrical model of the vessel structure structure using 2 parabolas - Foracchia [7]	97,5%
Vessels direction matched filter - Youssif et al [25]	98,8%

Table 6.3: Optic disk detection results for the proposed and literature methods with the Stare dataset.

This table shows a significant improvement of the results between a simple application of the sobel operator and the combination between sobel and the vessels mask to find the ROI. This modification has even better results comparing with the reference. In literature there are four models with a better performance for optic disk detection. However, the approaches followed for the authors are computational heavy. *Youssif et al* [25] developed an algorithm which needs on average 3.5 minutes for image in a computer with 2-GHz Intel Centrino 1.7 CPU and 512 Mb RAM. The geometrical model developed by *Foracchia* [7] spends 2 minutes on average by image in a computer with 2-GHz Intel Pentium IV CPU and 512 Mb RAM. *Frank ter Har* [21] and *Hoover and Goldbaum* [9] did not publish this data. Moreover, these algorithms do not have the ability to detect the optic disk radius and only do an estimation of its center based on the vessels orientation. The fovea is not detected in these four approaches.

6.1.4 Limitations of the model

The main limitation of the developed model consists in a relatively high sensitivity to other bright structures present in advanced stage of some diseases such as diabetic retinopathy. However, this problem was partially corrected with the combination between the sobel operator and the vessels mask for estimate de ROI. Figure 6.8 presents 2 images recovered with this new approach. Only the approaches based on the vessels direction have a high detection levels even with the presence of these structures. However they need a long average processing time by image. These kind of algorithms are not suitable to be integrated in Retmarker.

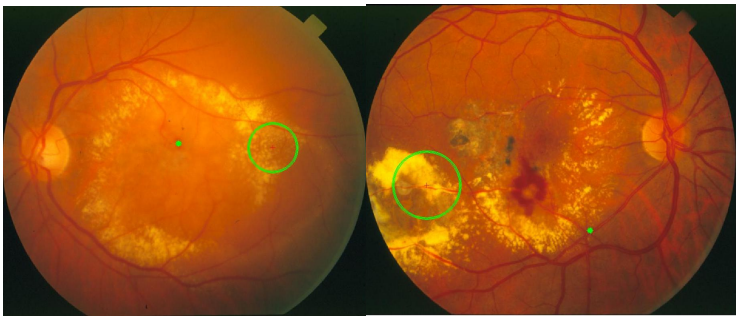

(a) im0002 with a failed detection

(b) im0049 with a failed detection

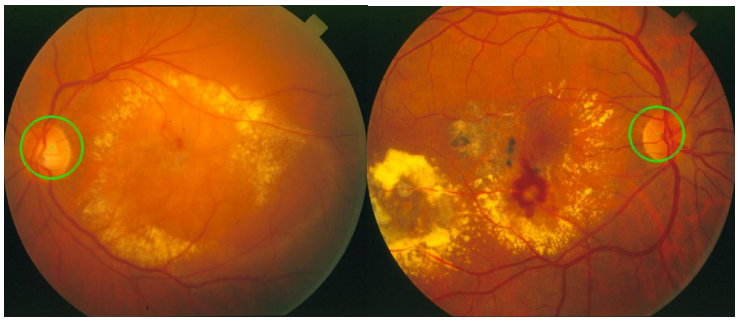

(c) im0002 recovered

(d) im0049 recovered

Figure 6.8: Two images of the Stare dataset recovered by the new approach implemented.

6.2 Key Performance Indicators

6.2.1 Implementation

A matlab interface was created to start the process (Figure 6.9) with the requirements mentioned in section 5.2 of the chapter 5. It uses XML files to store the selected settings in the hard drive and the same can be loaded to reload the options chosen. This was implemented using the xml toolbox of matlab.

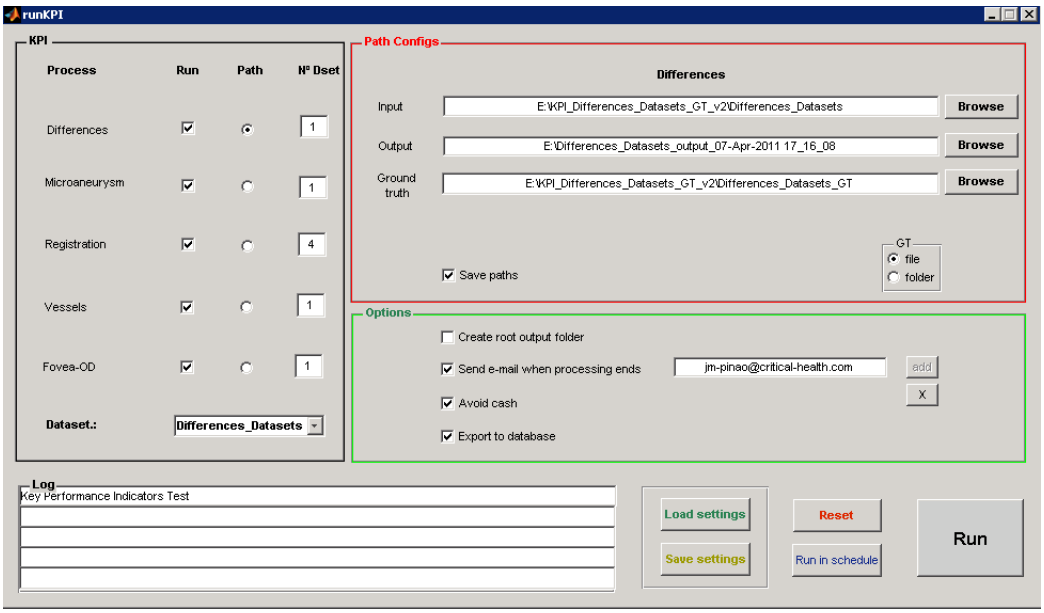

Figure 6.9: Matlab interface to start the KPI process.

A layer created in matlab was implemented to export all the processing results to the microsoft sql server database. This layer was created using the database toolbox of the matlab.

The application to analyse de results was developed using Microsoft Visual Studio development environment. A multilayer architecture was implemented during the development of the c# application to analyse the KPI. This architecture consists in three layers (Figure 6.10). The data access layer only reads data from the database and send it to the business logic layer in a encapsulated way using the models. The business logic layer receives the encapsulated data from the data access layer and compiles the information

to be showed in the user interface layer. This last layer only has as function interacts with the user and shows the information of interest.

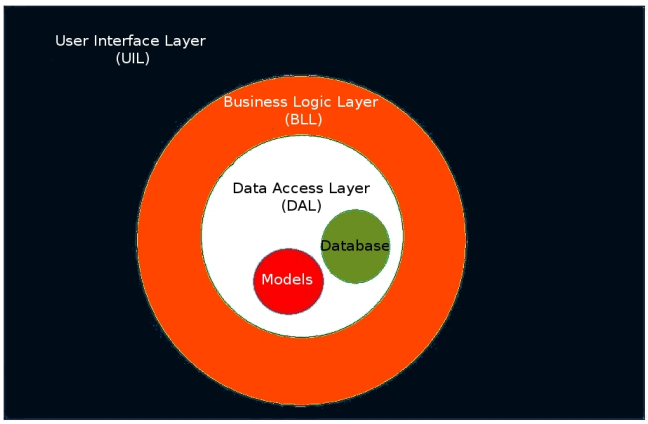

Figure 6.10: Architecture scheme for the c# application.

Figure 6.11 shows the window with the information for all processings in the database. It is observed the search box (1), a table with the processings where is possible generates a report for each one or delete them (2), a panel with the log of the selected processing in the table (3) and the information with how many runs each one has (4).

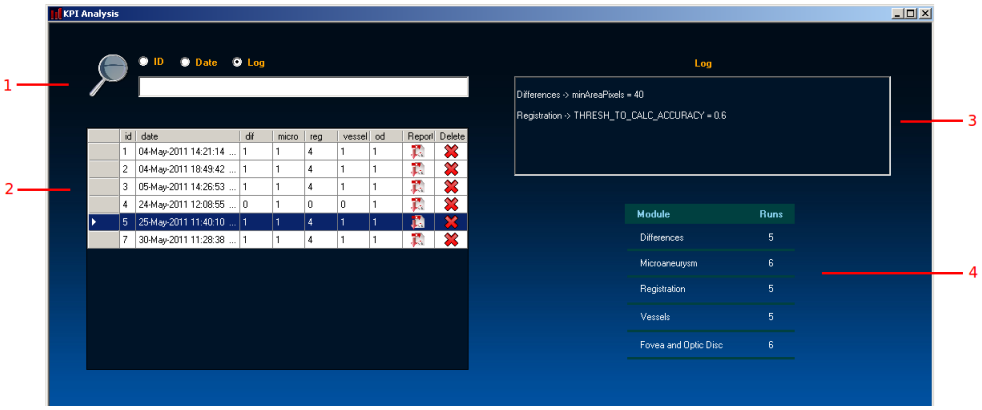

Figure 6.11: Overall window with the database data.

Each module has two respective windows. The figure 6.12a compares two processings with the differences module (1) selected in (2) and returns the *delta* between each parameter (3). Each module has a text processor to store all the conclusions taken (4). The other (figure 6.12b) allows sorting each parameter of all processings results by ascending or descending order.

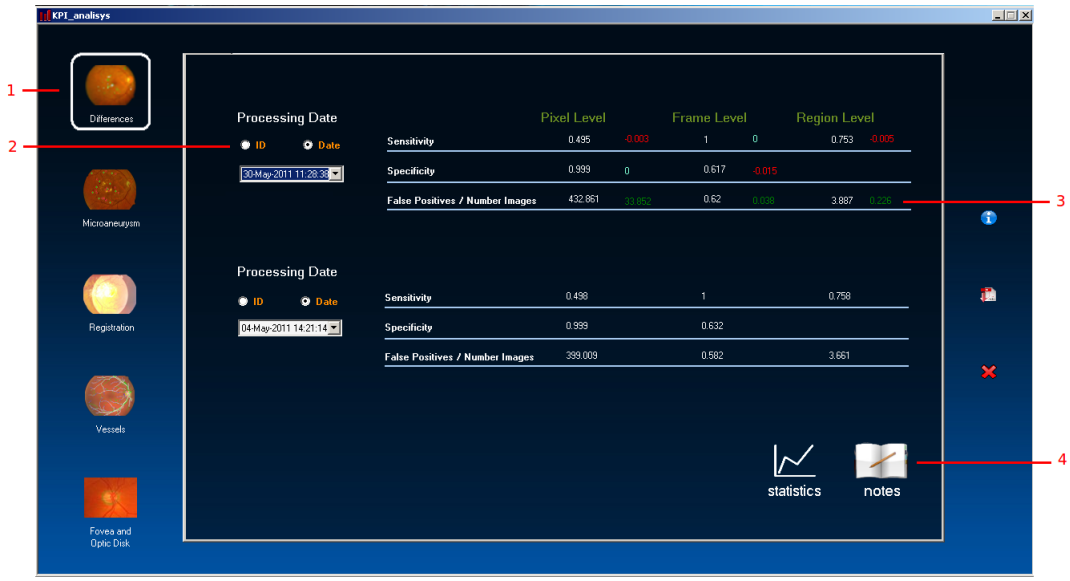

(a) Comparison between two processings.

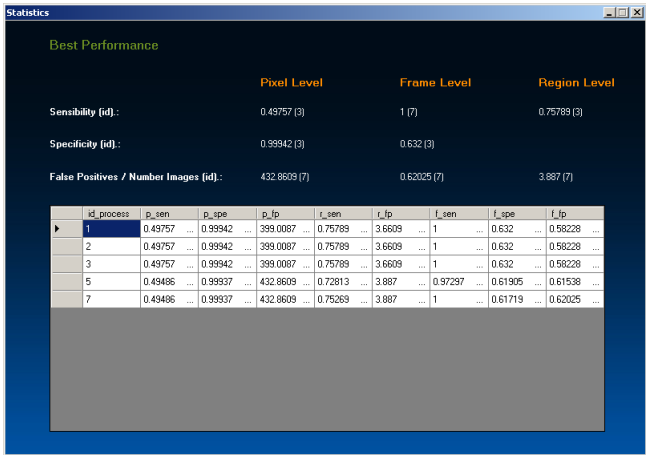

(b) Overall analysis.

Figure 6.12: Data analysis for the differences module.

The microaneurisms's window contains two panels, one for each selected processing (1) (2), with the information about the microaneurysms detected in each image of the dataset of test(Figure 6.13a) beyond the sensitivity, specificity and false positives per images.

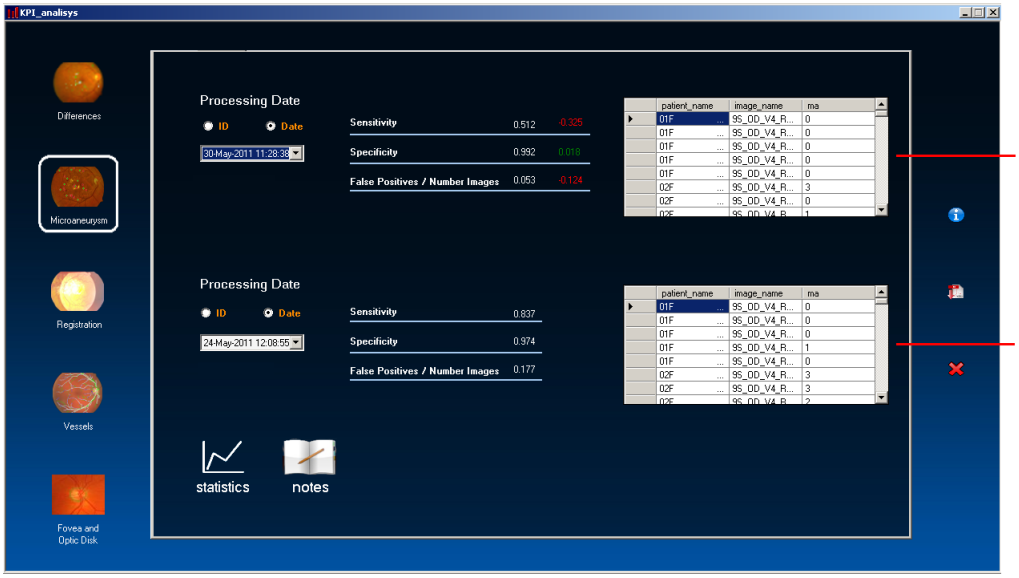

(a) Comparison between tow processings.

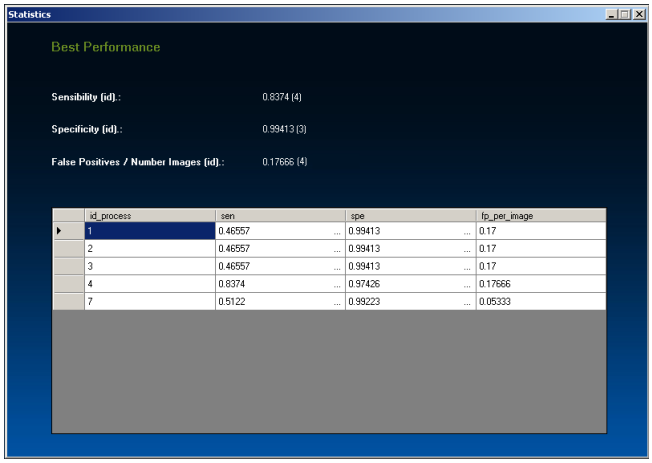

(b) Overall analysis.

Figure 6.13: Data analysis for the microaneurysms module.

All the charts were implemented with the MS chart available for .Net Framework 3.5. For the registration module are generated two charts (Figure 6.14b) where there is a comparison between the two processings selected in the main window. The axis are the percentage of images successfully registered for each value of threshold. The chart (1) shows the results with the V1 method and chart (2) the results for V2. In this case the results were equal.

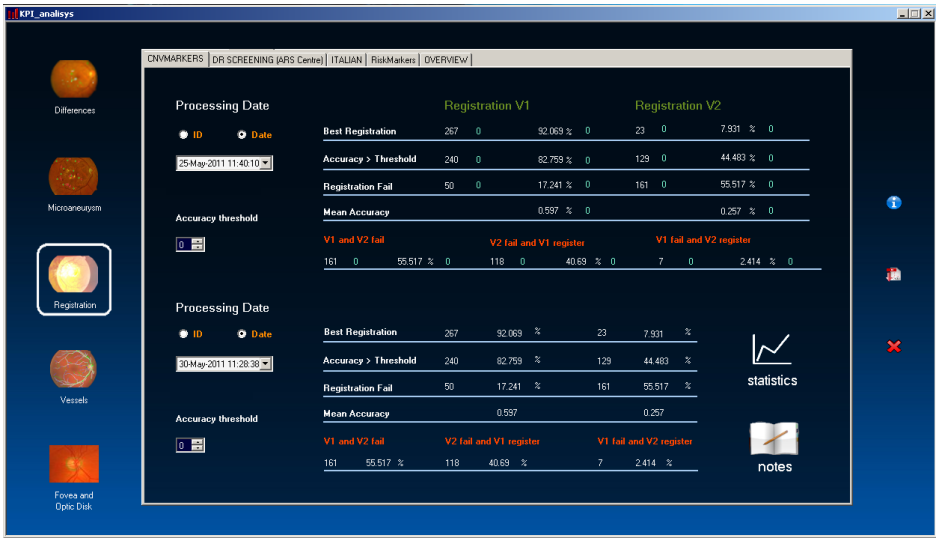

(a) Comparison between two processings.

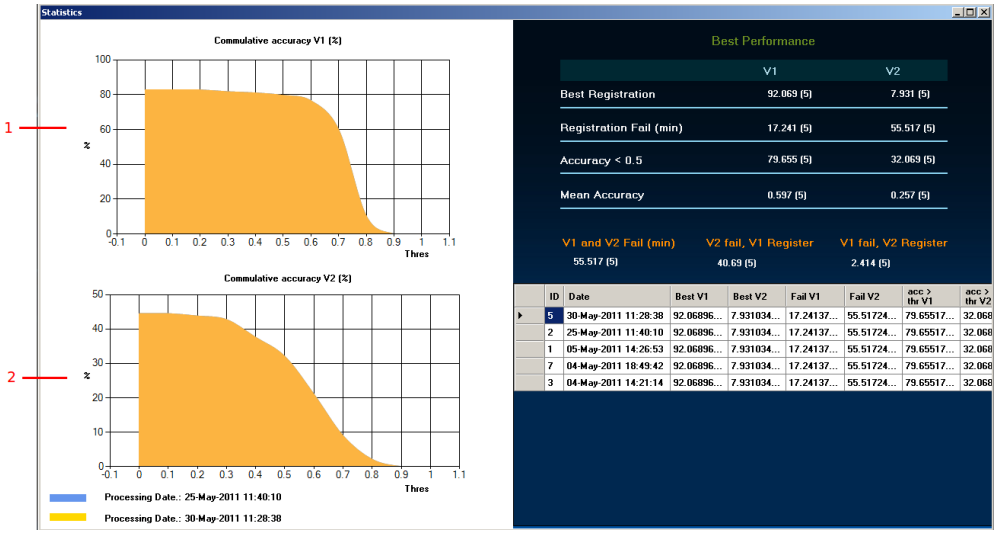

(b) Overall analysis.

Figure 6.14: Data analysis for the registration module.

As for microaneuryms, vessels module only presents as KPI the sensitivity, specificity and the number of false positives per image (Figure 6.15).

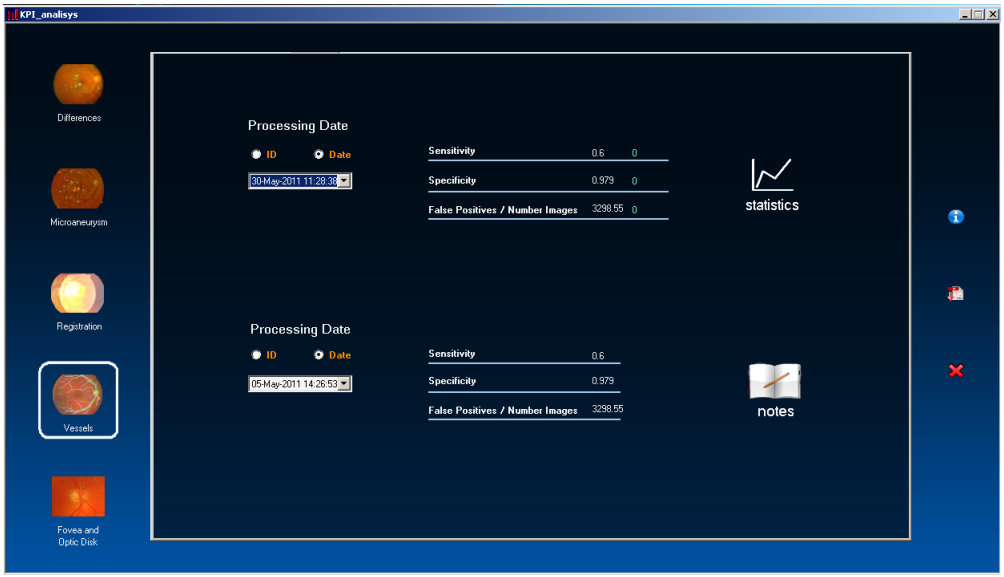

(a) Comparison between two processings

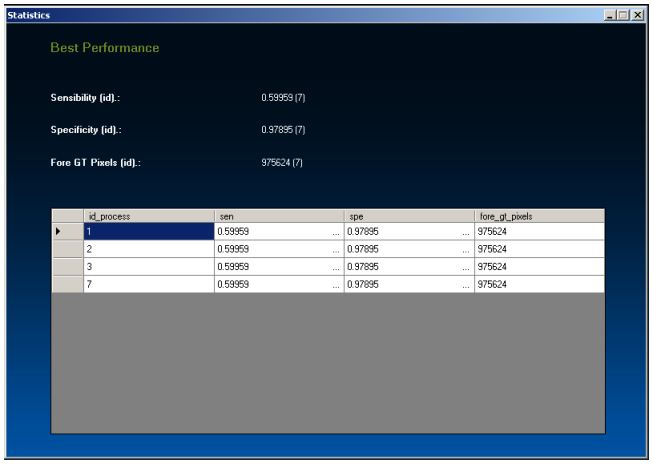

(b) Overall analysis

Figure 6.15: Data analysis for the vessels module.

For fovea and optic disk module the charts show for the processings selected, the percentage of optic disks (1) and foveas (2) detected for different values of threshold. In this case the blue area corresponds to the developed algorithm for the fovea and optic disk detection and the yellow to the algorithm of Retmarker (Figure 6.16b).

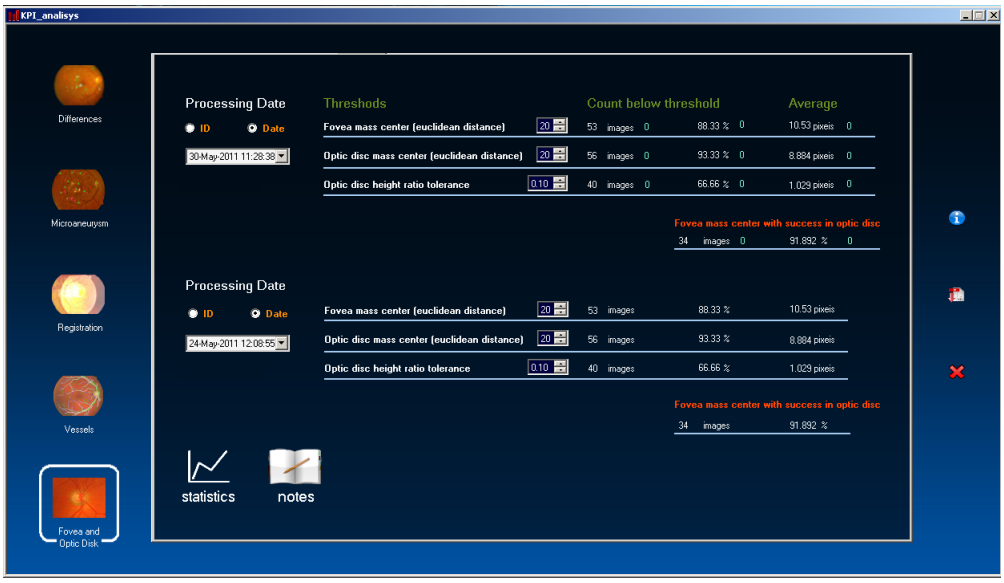

(a) Comparison between two processings.

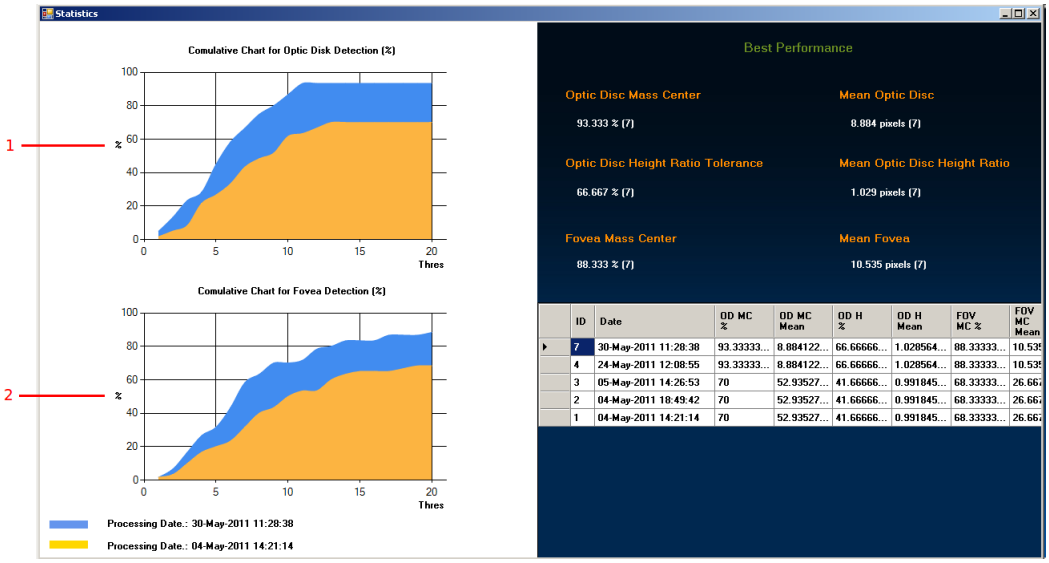

(b) Overall analysis.

Figure 6.16: Data analysis for the fovea and optic disk module.

Chapter 7

Conclusions And Future Work

A new fully automatic model is proposed in this work to detect the fovea and optic disk center and radius in retinal images. Comparing with the literature, this method is one of the few that detects the center and the radius of the optic disk. This algorithm was developed with a particular concern to be a fast method and to keep interesting levels of detection performance. For all the datasets tested, this proposed methodology revealed to be a powerful tool to detect the structures mentioned. This algorithm consists in a 3 main steps:

1. A pre-processing of the source image.
2. Detection of the optic disk with the Hough transform.
3. Detection of the fovea based in the optic disk position.

The validation tests proved that this model is capable of performing a reliable detection of the optic disk and fovea. Comparing with the reference model, and others in the literature, this is one of the methods with a better ratio between a good detection and a short time. Most of the tests demonstrated better indicators comparing with the reference and even with the majority of the methods presented in literature. The methods observed in literature which claim a better accuracy for the public Stare dataset have the detection based in the vessels tracing which invalidates the optic disk radius detection. Only estimate the optic disk center. Moreover, all of them are computational heavier. All the features shows that this model is a strong contribution to be applied in an automatic approach for screening programmes in the future. A paper about this work was already accepted for the VipIMAGE 2011 - III ECCOMAS Thematic Conference on Computational Vision and Medical Image Processing.

The fully automatic Key Performance Indicators process proposed in this thesis has been successful implemented in Critical Health. The automation was done using some technologies such as matlab, c#, microsoft sql server and xml. The thresholds present in Retmarker algorithms already have been tested with the goal of improving their performance.

To finalize the evaluation, a higher number of tests should be done in the future to understand the real effect of the combination between the result of the sobel operator with the vessels mask in the calculation of the ROI. However, the preliminary results are promising and seem to have potential to improve the performance.

Bibliography

[1] K. Akita and H. Kuga. A computer method of understanding ocular fundus images. *Pattern Recognition*, 15(6):431–443, 1982.

[2] J. Canny. A Computational Approach to Edge Detection. *IEEE Transactions on Pattern Analysis and Machine Intelligence*, PAMI-8(6):679–698, Nov. 1986.

[3] F. G. Chanwimaluang T. An efficient algorithm for extration of anatomical structures in retinal images. *IEEE international conference on image processing*, pages 1093–6, 2003.

[4] O. Chutatape. Automatic location of optic disk in retinal images. *Proceedings 2001 International Conference on Image Processing (Cat. No.01CH37205)*, pages 837–840.

[5] T. Cootes. Active Shape Models-Their Training and Application. *Computer Vision and Image Understanding*, 61(1):38–59, Jan. 1995.

[6] S. Deans. Hough transform from the Radon transform. *Pattern Analysis and Machine Intelligence, IEEE Transactions on*, 6(2):185–188, 1981.

[7] M. Foracchia, E. Grisan, A. Ruggeri, and S. Member. Detection of Optic Disc in Retinal Images by Means of a Geometrical Model of Vessel Structure. *IEEE Trans Med Imaging 2004*, 23:1189–1195, 2004.

[8] R. Haddad and A. Akansu. A class of fast Gaussian binomial filters for speech and image processing. *Signal Processing, IEEE Transactions on*, 39(3):723–727, Mar. 1991.

[9] A. Hoover and M. Goldbaum. Locating the optic nerve in a retinal image using the fuzzy convergence of the blood vessels. *Medical Imaging, IEEE Transactions on*, 22(8):951–958, Aug. 2003.

[10] H. F. Jelinek, C. Depardieu, C. Lucas, D. J. Cornforth, W. Huang, and M. J. Cree. Towards Vessel Characterisation in the Vicinity of the Optic Disc in Digital Retinal Images. *Image and Vision Computing New Zealand 2005*, 2005.

[11] D. Kavitha and S. Devi. Automatic detection of optic disc and exudates in retinal images. *Proceedings of 2005 International Conference on Intelligent Sensing and Information Processing, 2005.*, pages 501–506, 2005.

[12] M. Lalonde, M. Beaulieu, and L. Gagnon. Fast and robust optic disc detection using pyramidal decomposition and Hausdorff-based template matching. *IEEE transactions on medical imaging*, 20(11):1193–200, Nov. 2001.

[13] H. Li. Boundary detection of optic disk by a modified ASM method. *Pattern Recognition*, 36(9):2093–2104, Sept. 2003.

[14] F. Mendels, C. Heneghan, and J. Thiran. Identification of the optic disk boundary in retinal images using active contours. In *Proceedings of the Irish Machine Vision and Image Processing Conference*, pages 103–115. Citeseer, 1999.

[15] M. Niemeijer, M. D. Abràmoff, and B. van Ginneken. Segmentation of the optic disc, macula and vascular arch in fundus photographs. *IEEE transactions on medical imaging*, 26(1):116–27, Jan. 2007.

[16] A. Osareh, M. Mirmehdi, B. Thomas, and R. Markham. Colour Morphology and Snakes for Optic Disc Localisation. *The 6th medical image understanding and analysis conference*, pages 21–24, 2002.

[17] a. Osareh, M. Mirmehdi, B. Thomas, and R. Markham. Comparison of colour spaces for optic disc localisation in retinal images. *Object recognition supported by user interaction for service robots*, 1:743–746, 2002.

[18] N. Otsu. A Threshold Selection Method from Gray-Level Histograms. *IEEE Transactions on Systems, Man, and Cybernetics*, 9(1):62–66, 1979.

[19] S. Sekhar, W. Al-Nuaimy, and A. Nandi. Automated localisation of retinal optic disk using hough transform. *Biomedical Imaging: From Nano to Macro, 2008. ISBI 2008. 5th IEEE International Symposium on*, pages 1577–1580, 2008.

[20] C. Sinthanayothin, J. F. Boyce, H. L. Cook, and T. H. Williamson. Automated localisation of the optic disc, fovea, and retinal blood vessels from digital colour fundus images. *The British journal of ophthalmology*, 83(8):902–10, Aug. 1999.

[21] F. ter Haar. Automatic localization of the optic disc in digital colour images of the human retina. *Utrecht University*, 2005.

[22] K. W. Tobin, Jr. Characterization of the optic disc in retinal imagery using a probabilistic approach. *Proceedings of SPIE*, pages 61443F–61443F–10, 2006.

[23] T. Walter. Segmentation of color fundus images of the human retina: Detection of the optic disc and the vascular tree using morphological techniques. *Medical Data Analysis*, pages 282–287, 2001.

[24] D. Williams and M. Shah. A fast algorithm for active contours and curvature estimation. *CVGIP: Image understanding*, 55(1):14–26, 1992.

[25] a. R. Youssif, a. Z. Ghalwash, and a. R. Ghoneim. Optic disc detection from normalized digital fundus images by means of a vessels' direction matched filter. *IEEE transactions on medical imaging*, 27(1):11–8, Jan. 2008.

[26] X. Zhu and R. M. Rangayyan. Detection of the optic disc in images of the retina using the Hough transform. *Conference proceedings : ... Annual International Conference of the IEEE Engineering in Medicine and Biology Society. IEEE Engineering in Medicine and Biology Society. Conference*, 2008:3546–9, Jan. 2008.

Appendix A

Key Performance Indicators Report

The report was generated using the MigraDoc and PDFsharp libraries for C#.

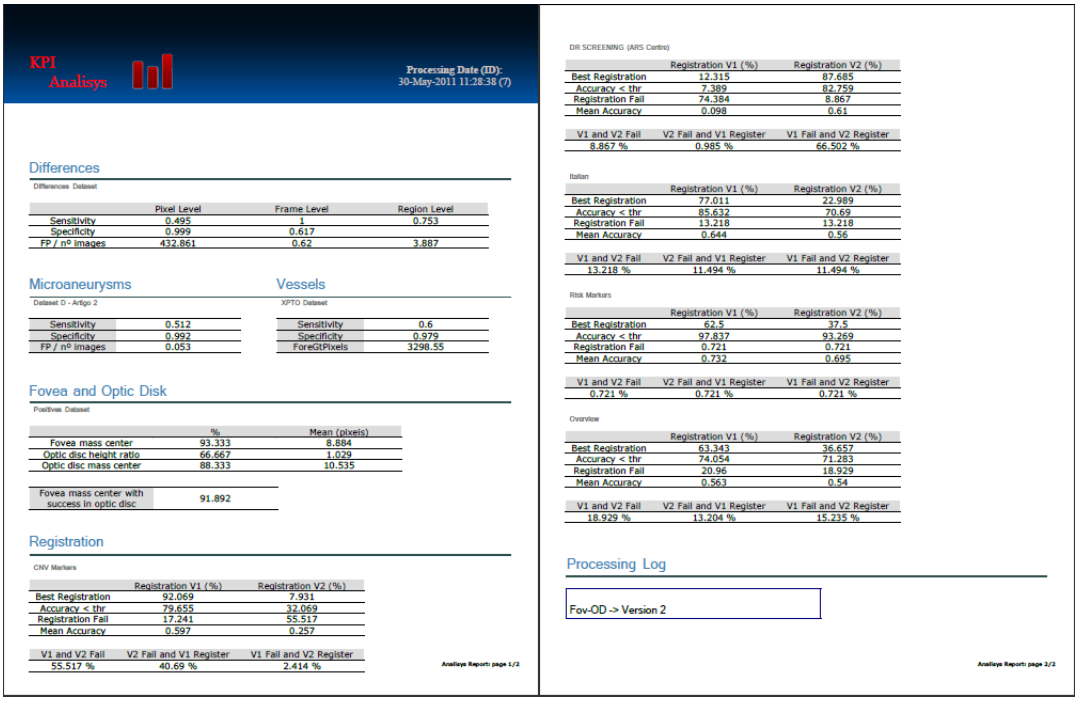

KPI Analisys

Processing Date (ID):
30-May-2011 11:28:38 (7)

Differences

Differences Dataset

	Pixel Level	Frame Level	Region Level
Sensitivity	0.495	1	0.753
Specificity	0.999	0.617	
FP / nº images	432.861	0.62	3.887

Microaneurysms

Dataset D - Artigo 2

Sensitivity	0.512
Specificity	0.992
FP / nº images	0.053

Vessels

XPTO Dataset

Sensitivity	0.6
Specificity	0.979
ForeGtPixels	3298.55

Fovea and Optic Disk

Positives Dataset

	%	Mean (pixels)
Fovea mass center	93.333	8.884
Optic disc height ratio	66.667	1.029
Optic disc mass center	88.333	10.535

Fovea mass center with success in optic disc	91.892

Registration

CNV Markers

	Registration V1 (%)	Registration V2 (%)
Best Registration	92.069	7.931
Accuracy < thr	79.655	32.069
Registration Fail	17.241	55.517
Mean Accuracy	0.597	0.257

V1 and V2 Fail	V2 Fail and V1 Register	V1 Fail and V2 Register
55.517 %	40.69 %	2.414 %

Analisys Report: page 1/2

DR SCREENING (ARS Centro)

	Registration V1 (%)	Registration V2 (%)
Best Registration	12.315	87.685
Accuracy < thr	7.389	82.759
Registration Fail	74.384	8.867
Mean Accuracy	0.098	0.61

V1 and V2 Fail	V2 Fail and V1 Register	V1 Fail and V2 Register
8.867 %	0.985 %	66.502 %

Italian

	Registration V1 (%)	Registration V2 (%)
Best Registration	77.011	22.989
Accuracy < thr	85.632	70.69
Registration Fail	13.218	13.218
Mean Accuracy	0.644	0.56

V1 and V2 Fail	V2 Fail and V1 Register	V1 Fail and V2 Register
13.218 %	11.494 %	11.494 %

Risk Markers

	Registration V1 (%)	Registration V2 (%)
Best Registration	62.5	37.5
Accuracy < thr	97.837	93.269
Registration Fail	0.721	0.721
Mean Accuracy	0.732	0.695

V1 and V2 Fail	V2 Fail and V1 Register	V1 Fail and V2 Register
0.721 %	0.721 %	0.721 %

Overview

	Registration V1 (%)	Registration V2 (%)
Best Registration	63.343	36.657
Accuracy < thr	74.054	71.283
Registration Fail	20.96	18.929
Mean Accuracy	0.563	0.54

V1 and V2 Fail	V2 Fail and V1 Register	V1 Fail and V2 Register
18.929 %	13.204 %	15.235 %

Processing Log

Fov-OD -> Version 2

Analisys Report: page 2/2

Figure A.1